AFRL-AFOSR-VA-TR-2023-0253

A Multifunctional Materials-by-Design Approach to Ignition Desensitization

Xiaowei Zeng
University of Texas at San Antonio
One Utsa Circle
San Antonio, TX, 78249-1130
US

01/12/2023
Final Technical Report

Air Force Research Laboratory
Air Force Office of Scientific Research
Arlington, Virginia 22203
Air Force Materiel Command

REPORT DOCUMENTATION PAGE

PLEASE DO NOT RETURN YOUR FORM TO THE ABOVE ORGANIZATION.

1. REPORT DATE	2. REPORT TYPE	3. DATES COVERED	
20230112	Final	START DATE 20160515	END DATE 20200314

4. TITLE AND SUBTITLE
A Multifunctional Materials-by-Design Approach to Ignition Desensitization

5a. CONTRACT NUMBER	5b. GRANT NUMBER	5c. PROGRAM ELEMENT NUMBER
	FA9550-16-1-0204	61102F
5d. PROJECT NUMBER	**5e. TASK NUMBER**	**5f. WORK UNIT NUMBER**

6. AUTHOR(S)
Xiaowei Zeng

7. PERFORMING ORGANIZATION NAME(S) AND ADDRESS(ES)
University of Texas at San Antonio
One Utsa Circle
San Antonio, TX 78249-1130
US

8. PERFORMING ORGANIZATION REPORT NUMBER

9. SPONSORING/MONITORING AGENCY NAME(S) AND ADDRESS(ES)	10. SPONSOR/MONITOR'S ACRONYM(S)	11. SPONSOR/MONITOR'S REPORT NUMBER(S)
Air Force Office of Scientific Research 875 N. Randolph St. Room 3112 Arlington, VA 22203	AFRL/AFOSR RTA1	AFRL-AFOSR-VA-TR-2023-0253

12. DISTRIBUTION/AVAILABILITY STATEMENT
A Distribution Unlimited: PB Public Release

13. SUPPLEMENTARY NOTES

14. ABSTRACT
Next-generation aircraft will increasingly make use of internal carriages in order to reduce radar cross-section and drag. These internal carriages place additional volume and safety constraints on munitions designers, which ends up driving a need for novel energetic materials with high energy density and low sensitivity. Over the last few decades, energetic materials designers have discovered how to tune the sensitivity of polymer-bonded explosives (PBXs) by adjusting binder material and volume fraction, crystal composition and morphology, and porosity. With the exception of porosity, a decrease in sensitivity nearly always comes at the expense of performance metrics, e.g. detonation velocity and pressure. Learning how to improve sensitivity without adversely impacting performance may lead to a suite of munitions capable of better meeting the design constraints imposed by next-generation aircraft. The primary objective of the proposed research is to demonstrate the efficacy of a microstructural design strategy focused on multifunctional tailoring of the binder phase in reducing the sensitivity of energetic materials without adversely affecting detonation performance. It is hypothesized that the properties of the binder phase may be altered in such a way as to reduce the number and magnitude of energy localizations while simultaneously shielding energetic crystals from damage generated by a thermomechanical insult. This hypothesis will be evaluated through the manufacture and characterization of an inert simulate of a polymer

15. SUBJECT TERMS

16. SECURITY CLASSIFICATION OF:			17. LIMITATION OF ABSTRACT	18. NUMBER OF PAGES
a. REPORT U	b. ABSTRACT U	c. THIS PAGE U	UU	34

19a. NAME OF RESPONSIBLE PERSON	19b. PHONE NUMBER *(Include area code)*
CHIPING LI	426-8574

To:	technicalreports@afosr.af.mil
Subject:	Final Performance Report to Dr. Martin Schmidt
Project title:	A multifunctional materials-by-design approach to ignition desensitization
Grant number:	FA9550-16-1-0204 **Total award:** $360,000

Original PI: Dr. Justin W. Wilkerson
Texas A&M University (TAMU)
Email: wilkerson@tamu.edu Phone: (979) 862-6068

PI of Record: Dr. Xiaowei Zeng
University of Texas at San Antonio (UTSA)
Email: xiaowei.zeng@utsa.edu Phone: (210) 458-7698

Program Officer: Dr. Martin Schmidt
Dynamic Materials and Interactions
Email: martin.schmidt@us.af.mil Phone: (703) 588-8436

Project period: 5/15/16 – 3/14/20 (including a 10-month no-cost extension)

EXECUTIVE SUMMARY

Problem statement: Next-generation aircraft will increasingly make use of internal carriages in order to reduce radar cross-section and drag. These internal carriages place additional volume and safety constraints on munitions designers, which ends up driving a need for novel energetic materials with high energy density and low sensitivity. Over the last few decades, energetic materials designers have discovered how to tune the sensitivity of polymer-bonded explosives (PBXs) by adjusting binder material and volume fraction, crystal composition and morphology, and porosity. With the exception of porosity, a decrease in sensitivity nearly always comes at the expense of performance metrics, e.g. detonation velocity and pressure. Learning how to improve sensitivity without adversely impacting performance may lead to a suite of munitions capable of better meeting the design constraints imposed by next-generation aircraft.

Objective: The primary objective of the research is to demonstrate the efficacy of a microstructural design strategy focused on multifunctional tailoring of the binder phase in reducing the sensitivity of energetic materials without adversely affecting detonation performance. A secondary objective of the effort was to advance the state-of-the-art in predictive mesoscale modeling of PBXs.

Hypothesis: It is hypothesized that the properties of the binder phase, e.g. elastic constants, viscoelastic damping, and thermal conductivity, may be altered in such a way as to significantly reduce the number and magnitude of energy localizations while simultaneously shielding energetic crystals from damage generated by a thermomechanical insult.

Scope of work: The hypothesis was evaluated through the manufacture and characterization of an inert simulant of a polymer bonded explosive with varying concentrations of carbon nanotubes (CNTs) incorporated into the binder phase. Several thermomechanical properties will be experimentally determined, e.g. loss modulus, strain to fracture, and thermal conductivity. Advanced diagnostics techniques will be

utilized to provide time-resolved, full-field characterization of energy localizations generated by an impact load. It is hypothesized that the carbon nanotubes will provide additional dissipation pathways for this impact energy as well as quickly conduct heat away from energy localizations. Additionally, a two-scale, microscale-homogenized, mesoscale-explicit finite element framework has been developed to provide additional insights and parametric studies related to the sensitivity of this class of CNT-enhanced PBXs.

Summary of accomplishments and key findings:

- We developed a synthesis process to hot-press polymer bonded simulant (PBS) samples with high concentrations of carbon nanotubes (CNTs) and consistent dispersion.
- Our CNT-enhanced PBS has improved mechanical and thermal transport properties.
    - In particular, the thermal conductivity of CNT-enhanced PBS is double the baseline PBS.
    - Additionally, CNT-enhanced PBS is less susceptible to strain localization than the baseline.
- Drop-weight impact tests are conducted with moderately high-speed thermography
    - Our CNT-enhanced PBS develop five times cooler hot-spots than the baseline PBS.
    - Hot-spots in our CNT-enhanced PBS quench faster than in the baseline PBS.
    - The difference between our CNT-enhanced PBS and baseline PBS is amplified for by strain localizations, due to the fact that strong thermal gradients are generated.
- We developed a state-of-the-art mesoscale model to study thermomechanical response of PBS.
    - Deformation-induced heat generation from the following sources is accounted for:
        - viscoelastic dissipation in the binder phase
        - plastic work associated with dislocation motion on discrete slip planes
        - dynamic collapse of pores
        - frictional sliding along crystal-binder interfaces.
    - Thermal conduction is found to affect hot-spot temperatures at intermediate loading rates.
    - Strain localizations greatly amplify the effect of thermal conduction.
    - Collapse of pre-existing pores generates strain localization on multiple length scales.
    - Crystal arrangement has a greater effect on strain localization in PBX than crystal anisotropy.
    - That said, crystallography strongly affects hot-spot formation in single crystal RDX.
- We derived a number of analytic solutions and scaling laws that help generalize the findings.

Workforce development:

- On March 4th, 2020, Babak Ravaji, a PhD student supported by this grant, successfully defended his dissertation titled "Multiscale transient thermomechanics of heterogeneous materials" at Texas A&M University. Dr. Ravaji is now a postdoctoral research associate at the University of Houston working on crystal plasticity models for shock loading with Prof. Shailendra Joshi.
- On July 5th, 2020, Eliseo Iglesias, a PhD student supported by this grant, is scheduled to defend his dissertation tentatively titled "Full-field thermographic analysis of carbon nanotube reinforced composites with implications for polymer bonded explosives." Mr. Iglesias is a U.S. citizen and is pursuing career opportunities at DoD and DoE national laboratories.
- Tyler Rowe, a Masters student supported by this grant, successfully defended his thesis titled "Processing and Characterization of Carbon Nanotube Enhanced Energetic Materials," in July 2018. Mr. Rowe secured a position as an engineer in industry, after completing a summer as an AFRL Summer Scholar at Kirtland AFB in 2018.
- Kyle Fernandez, an undergraduate research assistant supported by this grant, graduated with his B.S. in Mechanical Engineering in 2018. Mr. Fernandez now works as an engineer for Southwest Research Institute (SwRI) in the Fire Technology Department.

- Zachary Huber successfully defended his Master's thesis in April 2018. Mr. Huber utilized the FLIR thermal camera acquired for this project to complete much of his thesis work. Mr. Huber is now a research engineer at Pacific Northwest National Laboratory (PNNL).
- Dr. Li-Qiang Lin, a postdoctoral research fellow supported by this grant, completed his training and is working as engineer at Molex, LLC in Detroit, MI.
- In 2017, Dr. Justin Wilkerson, the original PI of this grant, joined the Department of Mechanical Engineering at Texas A&M University as an Assistant Professor and the James J. Cain Faculty Fellow.
- In 2018, Dr. Xiaowei Zeng, the PI of record on this grant, received tenure from the Department of Mechanical Engineering at the University of Texas at San Antonio and was promoted to Associate Professor.

Archival publications stemming from this research effort:

1. Tyler Rowe. Processing and Characterization of Carbon Nanotube Enhanced Energetic Materials. Master's thesis, University of Texas at San Antonio, 2018.
2. Babak Ravaji. Multiscale transient thermomechanics of heterogeneous materials. Dissertation, Texas A&M University, 2020.
3. Eliseo Iglesias. Full-field thermographic analysis of carbon nanotube reinforced composites with implications for polymer bonded explosives. University of Texas at San Antonio, 2020. Dissertation in preparation.
4. Iglesias, E., Rowe, T., Fernandez, K., Chocron, S., Wilkerson, J.W. "Mechanical response of carbon nanotube reinforced particulate composites with implications for polymer bonded explosives." Manuscript in revision.
5. Ravaji, B., Wilkerson, J.W. "Anisotropic thermomechanical response of porous RDX single crystals." Manuscript in submission.
6. Ravaji, B., Wilkerson, J.W. "Localization of hot-spots in PBX: Crystal arrangement versus crystallography." Manuscript in preparation.
7. Ravaji, B., Wilkerson, J.W. "The role of binder conductivity on hot-spot formation in PBX." Manuscript in preparation.
8. Iglesias, E., Rowe, T., Fernandez, K., Chocron, S., Wilkerson, J.W. "Thermographic analysis of CNT-enhanced simulant explosives under impact loading." Manuscript in preparation.

Spin-off archival publications utilizing analytic solutions derived in this research effort:

9. Zachary Huber. Full-field experimental analysis of ductile and fatigue fracture and the accompanying thermal effects. Master's thesis, University of Texas at San Antonio, 2018.
10. Ravaji, B., Ali Lagoa, V., Delbo, M., Wilkerson, J.W. "Unraveling the mechanics of thermal stress weathering: rate-effects, size-effects, and scaling laws," J. Geophys. Res. Planets, 2019.
11. Ravaji, B., Ali Lagoa, V., Delbo, M., Wilkerson, J.W. "The Effect of Rotation Period on Thermal Stress Weathering." Lunar and Planetary Science Conference, Vol. 49, p. 2628, 2018.
12. Huber, Z., Wilkerson, J.W. "Revisiting the Sandia Fracture Challenge with deformation heating and strain localization considerations." Manuscript under review.
13. Dagro, A., Wilkerson, J.W. "A computational investigation of strain concentration in the brain in response to a rapid temperature rise." Manuscript in minor revision.
14. Dagro, A., Wilkerson, J.W., Thomas, T., Kalinosky, B., Payne, J. "Traumatic brain injury induced by pulsed microwave cavitation." Manuscript in submission.

Selected conference presentations and seminars:

1. J.W. Wilkerson, "The perplexing role of microstructure in extreme environments," ***Department of Aerospace Engineering Seminar***, Georgia Institute of Technology, Atlanta, GA, November 7, 2019.
2. J.W. Wilkerson, "Mesoscale modeling of pore growth in spall failure and pore collapse in energetic materials," ***Damage, Shock and Characterization University Outreach Workshop***, Los Alamos, NM, July 31, 2019.
3. B. Ravaji, J.W. Wilkerson (2019). The role of heat conduction on hot-spot formation in energetic materials. ***15th US National Congress on Computational Mechanics***, Austin, Texas, USA.
4. E. Iglesias, B. Ravaji, J.W. Wilkerson, Thermo-mechanical enhancement of polymer-bonded simulants. ***21st Biennial Conference of the APS Topical Group on Shock Compression of Condensed Matter (SHOCK19)***, Portland, Oregon, USA.
5. B. Ravaji, J. Wilkerson, Effects of nano-inclusions on the thermomechanical behavior of PBX, ***2019 Mach Conference,*** Annapolis, MD, April 3-5, 2019.
6. J. Wilkerson, B. Ravaji, L. Lin, E. Iglesias, T. Rowe, X. Zeng, Effects of nano-inclusions on the thermomechanical response of polymer bonded simulants (PBS), ***TMS 2019 Annual Meeting & Exhibition***, San Antonio, TX, March 10-14, 2019.
7. L. Lin, J. Wilkerson, X. Zeng, Computational investigation of crack-induced hot-spot beneration in energetic composites, ***TMS 2019 Annual Meeting & Exhibition***, San Antonio, TX, March 10-14, 2019.
8. L. Lin, J.W. Wilkerson, X. Zeng, Computational investigation of hot-spots generation by micocracks in carbon nanotube reinforced composite under dynamic loading, ***The 13th World Congress on Computational Mechanics***, New York, July 22-27, 2018.
9. J.W. Wilkerson, B. Ravaji, L. Lin, E. Iglesias, T. Rowe, X. Zeng, Effects of nano-inclusions on the thermomechanical response of polymer bonded simulants (PBS), ***The 13th World Congress on Computational Mechanics***, New York, July 22-27, 2018.
10. J.W. Wilkerson, "High-fidelity and reduced-order models for materials in extreme environments," ***Center for Mechanics of Solids, Structures and Materials Seminar***, University of Texas at Austin, TX, September 19, 2017.

Discoveries, inventions, or patent disclosures: None

TABLE OF CONTENTS

I. MATERIALS FOR POLYMER BONDED SIMULANTS

Constituent materials used in polymer bonded simulants (PBS):

The polymer binder consists of three components: hydroxyl-terminated polybutadiene (HTPB), plasticizer, and curing agent. HTPB is the preferred choice for rocket propellant and explosive material binder due to its enhancements to the bulk physical properties of PBXs. Rocket propellant takes on a similar structure to PBXs, with the polymer binder holding together an oxidizer and the metallic fuel. Typically, HTPB is known for having low viscosity, low glass transition temperature, high tensile strength, and chemical resistance. These properties make HTPB less susceptible to shock. Additionally, HTPB holds together relatively high solid volume fractions of crystal-phase material (typically ranging from 85-90%).

The plasticizer promotes plasticity and flexibility in the HTPB, and reduces brittle behavior. This contributes to the binder's ability to hold a larger amount of solid loading. HTPB bonds well with oil plasticizers. Bis(2-ethyhexyl) sebacate is the preferred plasticizer due to its compatibility with HTPB.

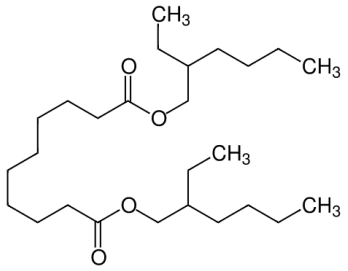

Figure 1.1: Chemical components of plasticizer, Bis(2- ethyhexyl) sebacate.

The curing agent is incorporated to initiate the curing of the binder material. HTPB reacts with isocyanates. Isocyanates react with compounds that contain free hydroxyl functional groups to form polyurethane polymer chains. One of the most widely used isocyanates, Tolylene di-isocyanate or TDI, was chosen to be the curing agent for the polymer binder. Together these components form the polyurethane polymer, HTPB.

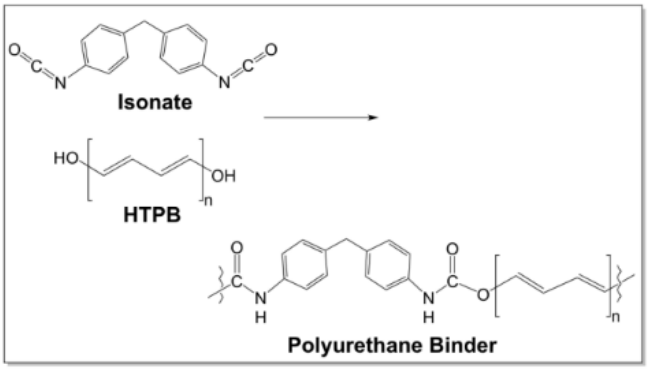

Figure 1.2: Chemical components of HTPB, where HTPB cures with isonate and the plasticizer to form the polymer binder system.

For handling in a university laboratory environment, a polymer-bonded simulant of explosive material is used for fabrication and testing. The polymer binder matrix is the same in both PBX and PBS, but PBS contains no explosive material. Instead, the explosive crystal-phase is substituted by sucrose, a common simulant of explosives.

Sucrose has a similar crystal morphology and size to that of HMX. Coarse grain HMX has been substituted by granulated sugar and fine HMX by powdered sugar in other experimental studies. Coarse sugar crystals,

700-1500 μm in size, were chosen as an explosive material simulant. Course sugar is easier to image and distinguish between binder and CNTs without the aid of electron microscopy.

Carbon nanotubes (CNTs) are composed of carbon atoms that are arranged in a defect free graphite plane that is rolled into a cylinder. The presence of the carbon-carbon bonds and the absence of defects in the plane allow CNTs to reach strength values that are unrivaled by other materials, with an average modulus of 1000 GPa and up to 200 GPa tensile strength. The benefit of CNTs is the ability to produce mechanically superior materials without adding a significant amount of weight. Due to their suite of impressive mechanical properties, CNTs are prime candidates for polymer-binder enhancement.

Table 1.1: Sucrose Size Distribution

Size	Mass (g)	Mass Fraction
> 500 microns	170.94	98.2%
> 425 microns	1.65	0.9%
> 250 microns	1.41	0.8%
< 250 microns	0.12	0.1%

CNTs exhibit high thermal conductivity values, up to 3000 W/m-K, thus are a prime candidate to increase the thermal conductivity of the material as well as the stiffness of the material. The increased thermal conductivity would allow the binder-phase of the polymer composite to effectively conduct heat away from the localized hot spots generated by a shock-impact.

In addition, CNTs contain extremely high aspect ratios, meaning that their surface area is large when compared to their volume. This enables the CNTs to enhance the load transfer of the material to the binder. CNTs can also, potentially desensitize PBXs without the adverse impact on the performance. The decrease in performance seen from other desensitization techniques (e.g., aluminization) stem from having to decrease the volume fraction of the explosive material in exchange for filler material. CNTs offer the added benefit of affecting properties even at low concentrations reducing the impact on the volume fraction percentage of the explosive material. An expected issue with adding CNTs is their tendency to agglomerate. Due to van der Waals forces, CNTs tend to clump together, and this clumping prevents harnessing the full impact of the CNTs. Steps exist to reduce agglomeration, but there will likely always be at least some clumping present. The expected benefits cannot be predicted using simple methods like the Rule of Mixtures (ROM) method. In order to maximize the benefits obtained from CNTs, proper dispersion is paramount. The main strategies to achieve this dispersion is through high frequency ultra-sonication in an alcohol bath, high shear rates stirring, and a pre-cure procedure designed to increase the viscosity of the polymer before the CNTs are added in to prevent the CNTs clumping once mixing begins. Material properties are shown in Table 1.2.

Table 1.2: Individual Material Properties

Material	Density (g/ml)	Size	Conductivity (W/m-k)
Hydroxyl terminated polybutadiene (HTPB)	0.913	-	0.23
Bis(2-ethylhexyl) sebacate (Plasticizer)	0.914	-	-
Tolylene- 2,4-discyanate (TDI)	1.214	-	-
Multi-walled carbon nanotubes	2.1	20-30 nm	>3000
Sucrose	1.5-1.6	850-1500 μm	0.2

All of the CNTs used for the PBS samples are multi-walled. The specific dimensions are 20-30 nm in outer diameter, 5-10 nm in inside diameter and 10-30 μm in length. The nominal composition of the PBS samples presented here is: 80% sucrose, 9% HTPB, 9% plasticizer, and 2% curing agent (20% binder). These baseline samples are designated as PBS 8001 and the binder enhanced samples, PBS 8001 + N% wt CNTs, signifying the amount of MWCNTs added by weight percentage.

II. MATERIAL PROCESSING AND SAMPLE PREPERATION

Processing of 3" X 2" X 1" polymer bonded simulant (PBS) samples:

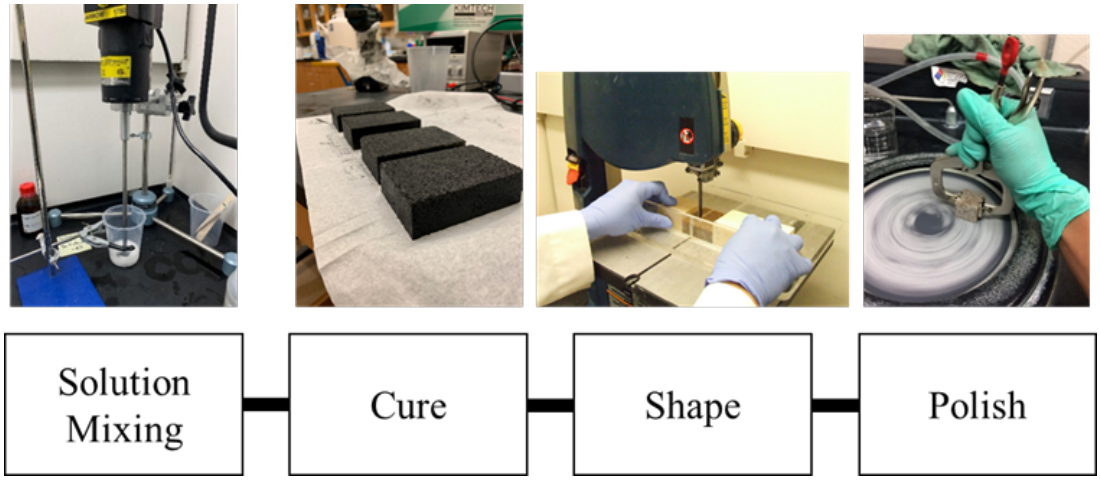

Figure 2.1: Synthesis procedure for fabricating 3" X 2" X 1" PBS bricks.

The synthesis process, shown in Fig. 2.1, begins with the solution mixing of HTPB, plasticizer, and CNTs with an Arrow 1750 laboratory mixer at 200 rpm for 30 minutes. During mixing, the mixture is placed on a hot plate which is kept at 60ºC. The solution mixing ensures a dispersion of the MWCNTs within the mixture. For another 30 minutes the solution mixing continues with the curing agent now added in. The last step is to slow pour the large grain sucrose and continue stirring until every crystal is coated with the mixture.

Figure 2.2: Single cavity aluminum mold for fabricating 3" X 2" X 1" PBS bricks.

Next, the mixture is poured into an aluminum mold coated with silicone lubricant and lined with heat resistant release film. In Fig. 2.2, the mold is accompanied by a corresponding aluminum plunger (also coated with silicone lubricant and lined with release film). This plunger is design to fit into the mold cavity and apply a constant load to the mixture during the curing process.

After mixing and prepping the aluminum mold is placed in a Carver 4126 heated hydraulic press. Here a load of 10-kips was applied and the platens were set to a temperature of 150ºC and left to cure for 75-wtinutes. During this process significant amount of leakage occurs from the aluminum molds. Due to the high pressure and temperature some of the polymer binder was found to leak from the creases of the mold. The loss in binder is characterized in 1.

Table 2.1: Binder Loss

Batch	Binder Loss [%]	Binder Loss[g]
PBS 8001	51.2	20.58
PBS 8001 + 1-wt% CNTs	34.5	14.14
PBS 8001 + 2-wt% CNTs	14.1	5.91
PBS 8001 + 3-wt% CNTs	24.2	10.71

The mass of the mixture pre-cure and post-cure were measured to calculate the total loss during cure. In Table 2.2, the true composition of the samples, detailed as mass fractions, are determined by assuming only the binder and MWCNTs leak from the mold during cure.

Table 2.2: Post-cure composition

Batch	Polymer Binder [%]	Sucrose [%]	CNTs [%]
PBS 8001	11.70	88.30	0
PBS 8001 + 1-wt% CNTs	14.73	84.29	0.97
PBS 8001 + 2-wt% CNTs	18.37	79.32	2.30
PBS 8001 + 3-wt% CNTs	16.45	80.45	3.10

As shown in Fig. 2.1, the mixture configuration after curing is a 3 by 2 by 1 inch bricks. These bricks cut into 1-inch cubes with a band saw and guide. The cubes are then further shaped using an overhead mill equipment with electronic translational readouts.

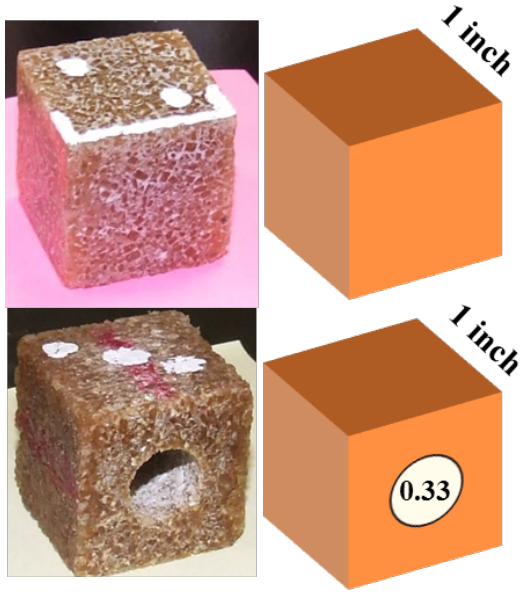

Figure 2.3: Final sample geometries. The top geometry is used in compression testing and drop-weight testing. The bottom geometry with a machined hole is used in drop-weight testing to induce strain localization.

The final step in the fabrication process is the surface treatment of the front face of the sample. This surface is the target the infrared camera will document. This surface is smoothed using silicon carbide discs of 320, 400, 600, 800, and 1200 grit size and polished with a silk polishing disc alongside a diamond-alcohol slurry. In order to ensure a constant emissivity to each sample a thin coat of black spray paint was applied.

Processing of 1" X 1" X 1" polymer bonded simulant (PBS) samples:

The MWCNTs are placed in an ethanol bath and then sonicated for 1 hour at 40-kHz and at a temperature of 60ºC. The aluminum mold is coated with mold release to assist in removing the samples safely after the cure. The mold release is a silicone lubricant that is non-curing, thermally stable, and inert.

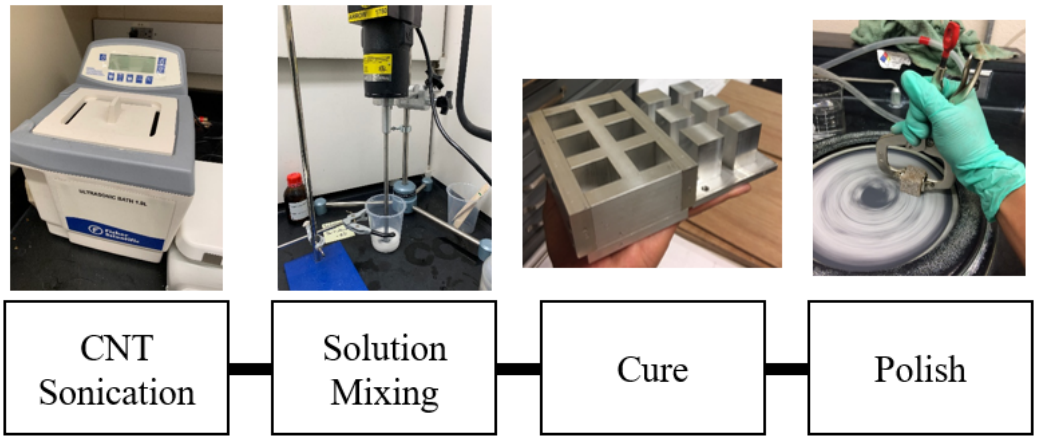

Figure 2.4: Schematic of synthesis procedure for fabricating 1" X 1" X 1" samples.

The binder composition mass-ratio of HTPB/Plasticizer/TDI was 5.37/5.37/1.02. The polymer material, HTPB, is heated to 60ºC on a hot plate while an electric mixer ensures effective mixing before cure. The plasticizer is then added and mixed in at 200 rpm for 10 minutes. Solution mixing is the preferred method for CNT dispersion due to being one of the most common methods for dispersing CNTs in a polymer matrix.

Table 2.3: Composition Break Down by Batch (mass in grams)

Batch	HTPB	Plasticizer	Curing Agent	Sucrose	CNTs
PBS-0	13.5	13.5	2.5	118	0
PBS + 1-wt% CNTs	13.5	13.5	2.5	118	1.5
PBS + 3-wt% CNTs	13.5	13.5	2.5	118	4.5

Before adding sucrose to the mixture 10% of the TDI is added and mixed in for an hour. The TDI will slowly begin curing the mixture just enough to slightly raise the viscosity. At this point, the sonicated CNTs are added in. Adding the CNTs directly to the mixture before the sugar was determined to be the most effective method for ensuring dispersion. The stirring rate is then increased to 400 rpm to assist in CNT dispersion via applying a high shear rate to the mixture. The increase of viscosity of the binder material assists in mitigating agglomeration issues among the CNTs.

Once the CNTs are incorporated, the remaining TDI and sucrose is added. Once the sucrose is thoroughly stirred, the mixture is poured into the mold. The aluminum mold used in for these samples were a rack-type mold with 6-cavities, each 1-inch in size.

The mixture cures using a heated hydraulic press. The press has two heated platens that can be adjusted to apply up to 30 kips. The hot press is set at a temperature of 70ºC and adjusted to apply a force between 7-kips and 10-kips. The samples cure in the hot press for 24 hours. After this period the samples are removed, weighed, and characterized to determine how much binder was lost due to the pressing.

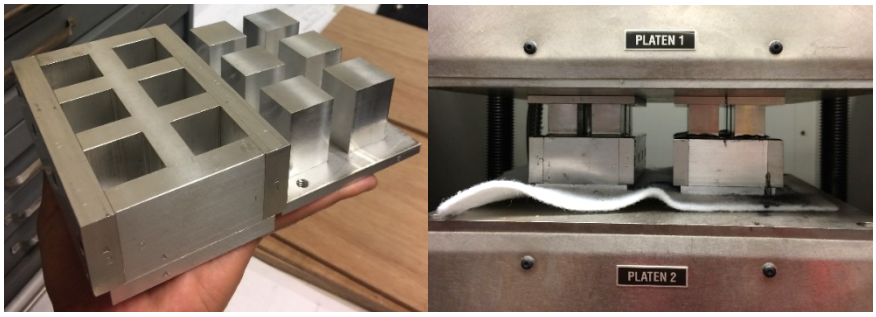

Figure 2.5: 6-cavity aluminum mold (left) and heated hydraulic press (right).

The samples consistently lose at least about 5-7% of their binder mass in the pressing. This means that PBS material has an 86% sucrose composition. The samples are next polished using a mechanical polishing wheel. They are generally subjected to a polish of four different grit-size polishing discs: 320, 600, 800, 1200, and finished with a polishing cloth with a diamond slurry.

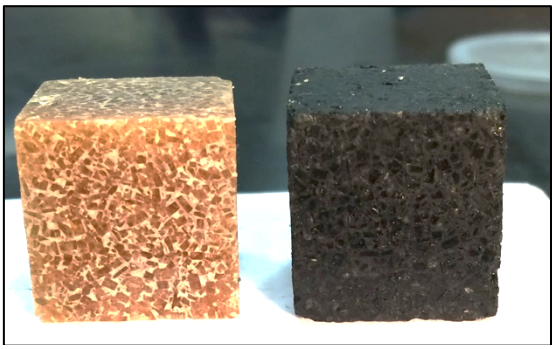

Figure 2.6: 1" X 1" X 1" polished samples of neat PBS on the left and CNT enhanced PBS on the right. Samples are shown prior to spray painting with flat black paint.

Three unique PBS samples types were created, their mass compositions are shown in Table 3. Note that these denote the *ideal* mass composition of the mixture, the actual mass of the samples change due to loss in pressing and curing. The loss is due to leakage that occurs during pressing portion of the procedure; this leakage is exclusively binder-loss since the creases within the aluminum mold are significantly smaller than the sucrose grains.

III. EXPERIMENTAL METHODOLOGIES

Drop weight testing with high speed thermography:

The drop weight apparatus, shown in Fig. 3.1, is approximately 25 inches (63.5 cm) in height. The weight of the flyer plate is approximately 1.5 kg and if dropped from the maximum allowable height can produce strain rates up to 200 s^{-1} (without any pulse shapers). In this apparatus, the goal is to test these soft polymer composites at relatively low-strain rates (less than 100 s^{-1}). Inspired by the work on impact testing of laminated carbon composites by Li and Liu, the apparatus was equipped with a pulse shaper and impact transfer block to appropriate test soft and brittle composite materials. In Figure 3.2, the pulse shaper, a 1-inch silicone cube, sits atop an impact transfer block. The drop weight first impacts the pulse shaper. This shaper makes the deceleration of the impactor less abrupt, which allows the test sample to experience a nearly uniform load without and reach a dynamic equilibrium state. Due to relatively small out-of-plane displacements, this setup allows the infrared camera to remain in focus with the front face of the sample during impact.

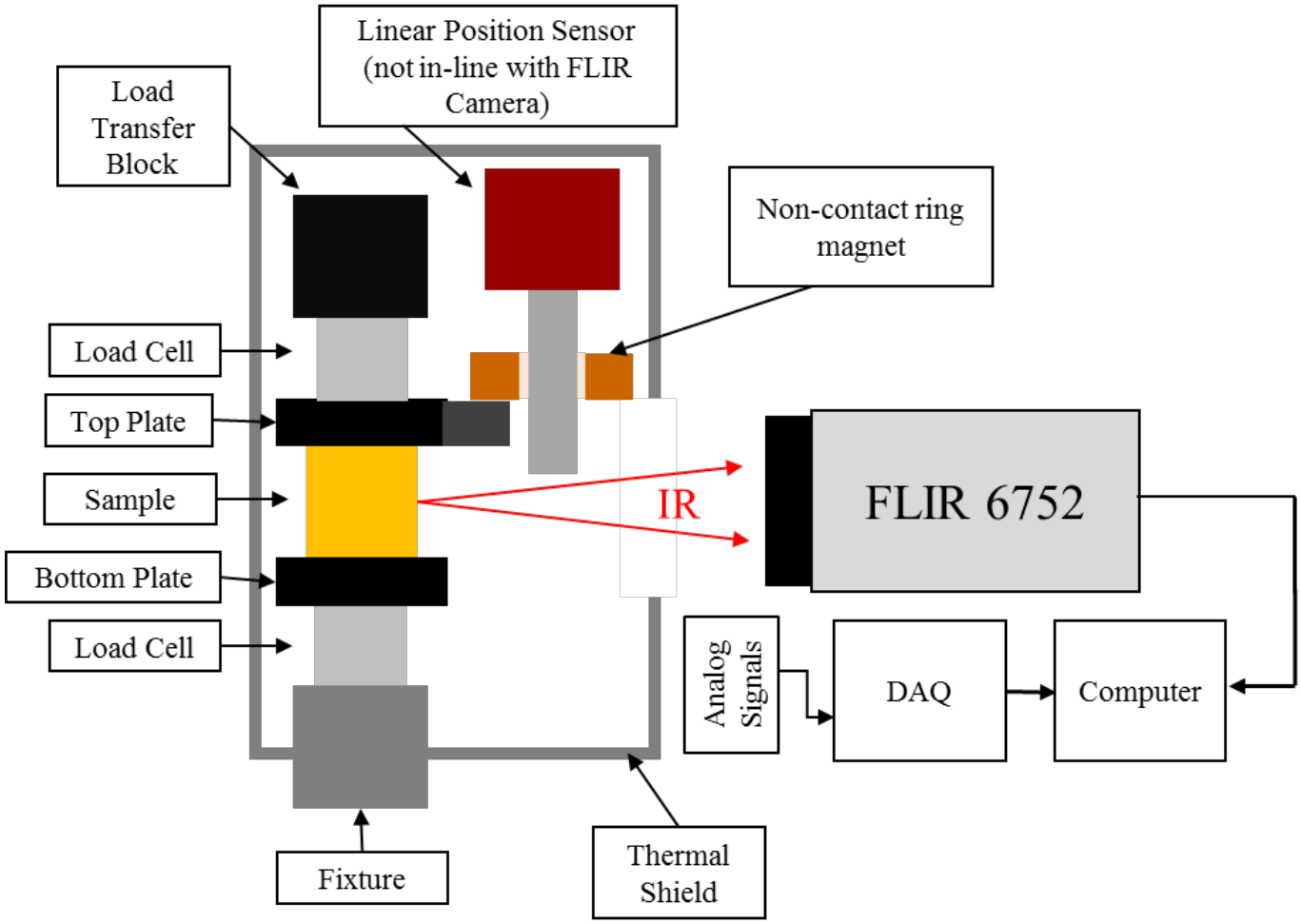

Figure 3.1: Schematic of in-situ infrared imaging during drop weight impact

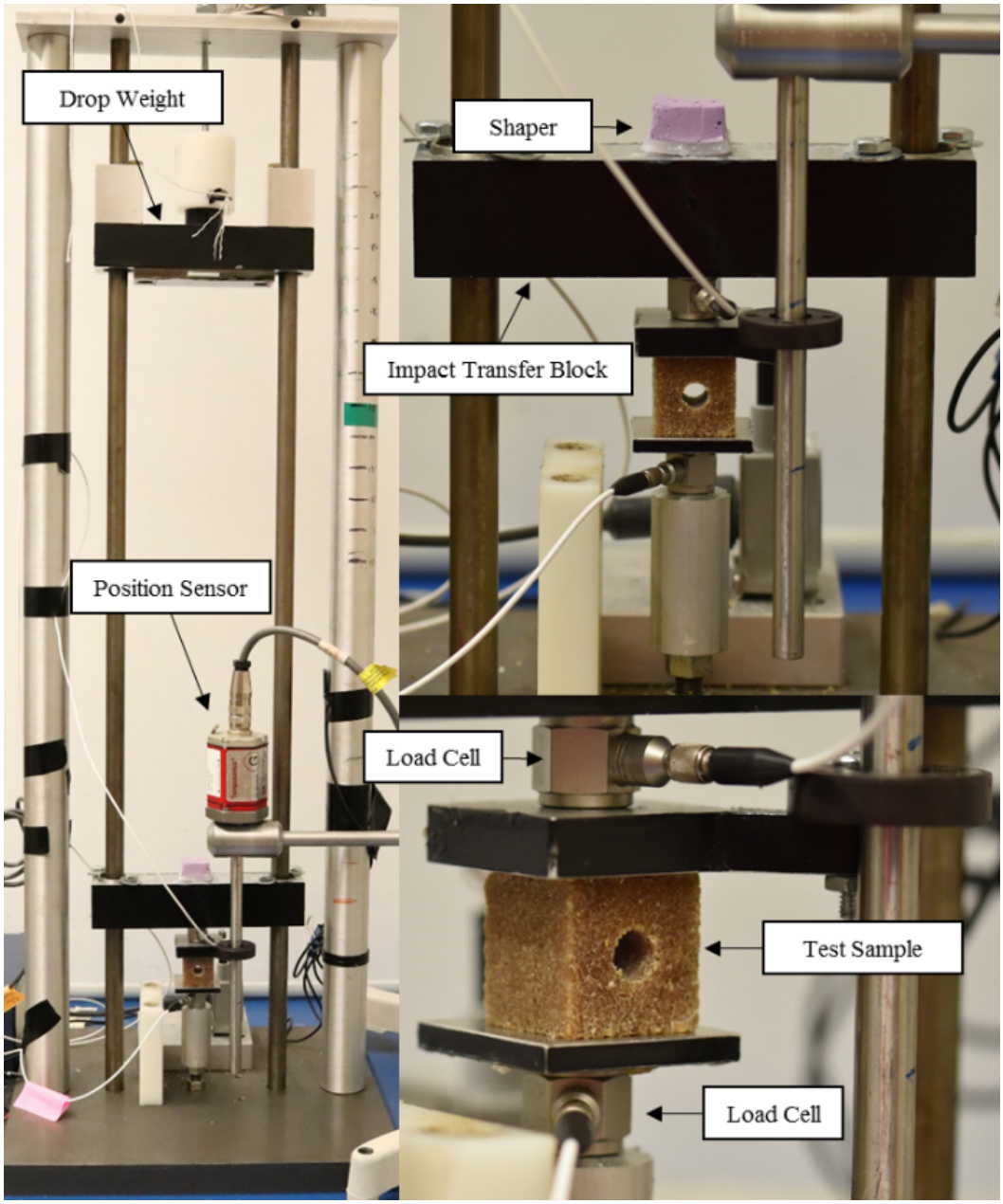

Figure 3.2: Drop weight tower apparatus

The apparatus is instrumented with a motion sensor, two load cells, a compact string potentiometer and a non-contact, magnetostrictive linear-position sensor (MLPS). The motion sensor, an E3T photoelectric sensor manufactured by OMRON ®, triggers the data acquisition of all instrumentation when the drop weight falls. This sensor is located 5 inches above the impact transfer block. The load cells are two piezoelectric transducers manufactured by PCB Piezotronics®. They are rated up to 1000lb (4.45 kN) of compressive static force. As seen in Fig. 3.2b, the load cells are situated above and below the test sample to conform an equilibrium state during impact. A SP2 wire potentiometer (TE Sensor solutions®) is used to measure the position of the drop weight and thus estimate entrance velocity. Lastly, a G-series magnetostrictive linear-position sensor, made by MTS Sensors®, is attached to the top plate that lies atop the test sample. The sensor measures the displacement of the top plate. This displacement can be interpreted as the global deformation the sample experiences under load. A loading rate can be estimated with the data from this sensor and additionally confirm a constant strain rate applied to the test sample.

High speed thermography:

The infrared imaging instrument employed in this study was a FLIR 6752 MWIR camera. As seen in Fig. 3.3, the camera is placed 0.5 m away from the test sample. Three thermal shields made of foam surround the impact test area to block stray infrared radiation from distorting the imaging. The approximate spatial resolution achieved was 150 µm/pixel (window size of 320 by 256 pixels). The highest frame rate available at the given resolution is 368 Hz. A typical impact event in this setup has a duration between 7 and 10 milliseconds. At the given frame rate the infrared camera can record up to three thermal data points per pixel within any given impact event.

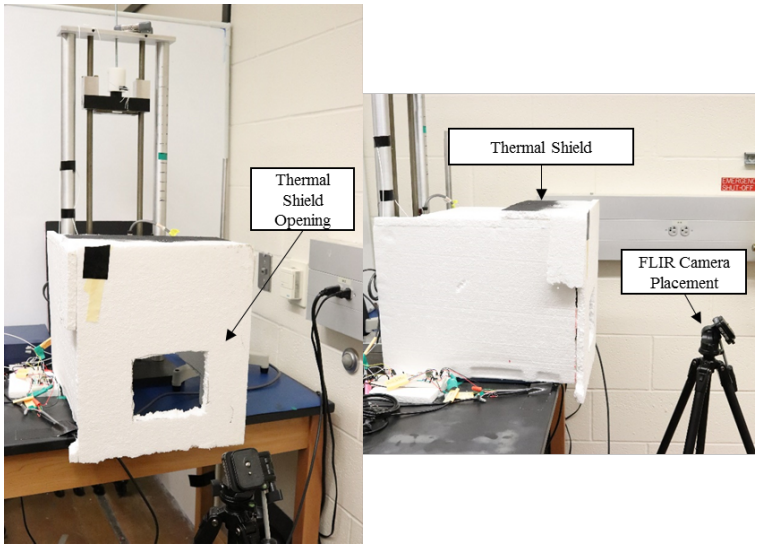

Figure 3.3: Infrared Camera Setup

Since the primary method of measure the temperature distribution any given sample under impact is through infrared radiation, emissivity becomes a factor. Stefan-Boltzmann's Law defines the relationship between the radiant energy and temperature of a 'grey-body' object. The infrared camera detects this radiant energy with a super-cooled ceramic material and outputs a voltage. This analog voltage signal, through an internal calibration and signal processing, is converted into a temperature reading.

Figure 3.4: Neat PBS 8001 sample spray painted with layer of flat enamel black paint to ensure an emissivity of approximately 0.95.

Most bodies can be considered a grey-bodies. Grey-bodies can reflect, transmit, and absorb a certain amount of radiation due to their surface opacity. Emissivity is a function of this surface effect; it is defined as the ratio between the true radiant energy emitted by a grey-body and the radiant energy of a blackbody at the

same temperature. All samples are coated with a thin, consistent, and flat coat of black paint. This should ensure an emissivity of approximately 0.96.

Measurement of thermal transport properties:

The thermal conductivity determination methodology presented here is based on the comparative cut method described in ASTM E1225 standard. The comparative cut method requires the use of two reference materials with a known thermal conductivity. The test sample is placed in between the two known reference samples. Using the temperature gradients measured on both reference samples at steady state, alongside their known thermal conductivity, the unknown bulk thermal conductivity is determined using Eq. 3.1:

$$k_{sample} = \frac{k_{ref}}{2}\frac{L_{sample}}{\Delta T_{sample}}\left(\frac{\Delta T_{ref1}}{L_{ref1}} + \frac{\Delta T_{ref1}}{L_{ref1}}\right) \qquad \text{Eq. 3.1}$$

The reference material, Titanium 6Al-4V Grade 5, was used in this study. This titanium alloy has a thermal conductivity value of 6.7 W/m-K. Minor discrepancies between the true and reported thermal conductivities of the reference material and possible heat loss, lead to an approximate error of 10% in the reported PBS 8001 thermal conductivity values, shown in Table 3.2.

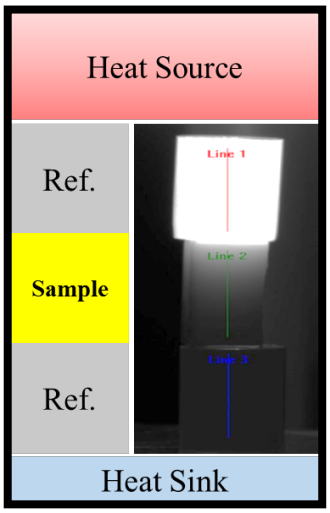

Figure 3.5: Schematic of comparative cut method. A SpotIR model 4085 infrared heater was used to apply heat to the reference sample. Two Titanium 6Al-4V Grade 5 reference bars were used. The heat sink is an aluminum block.

In Fig. 3.5, a model of the setup and infrared images capture is shown. The heat source for this experiment is provided by an infrared spot heater. The spot heater localizes the heat source to the top reference material and uniformly applies heat through only the top surface. The bottom reference material is in contact with a heat sink, a large piece of aluminum.

IV. KEY EXPERIMENTAL RESULTS

In order to assess the quality of samples within each batch-type multiple unconfined quasi-static compression tests were performed for PBS 8001, PBS 8001+1-wt% CNTs, PBS 8001+2-wt% CNTs, and PBS 8001+3-wt% CNTs batch types. At least three samples from each batch were tested for quality, consistency, and determination of several mechanical properties. Compressive modulus of elasticity, strength, strain-to-failure, porosity, and tangent modulus were the main properties of interest. Also of interest is determining the void volume fraction (VVF) or porosity of samples synthesized at different cure pressures. It has been observed in experiments that the sensitivity of the PBX tends to increase with higher porosity values. Additionally, porosity could be a critical variable in affecting the thermo-mechanical behavior of PBS samples.

In Table 4.1, the void volume fraction is listed for each sample type synthesized at two different cure pressures, 0 MPa and 5.8 MPa. The void volume fraction was determined by comparing the measured density of a sample with its actual density. The void volume fractions for the samples cured under atmospheric pressure for batch types PBS 8001 and PBS 8001+1-wt% CNTs are on average, 6.43% and 7%, respectively.

Table 4.1: Void Volume Fraction of PBS 8001

Batch	Cure Pressure (MPa)	Ideal Density (g/cm^3)	Actual Density (g/cm^3)	Void Volume Fraction
PBS 8001	0 MPa	1.45	1.34	6.43%
PBS 8001+ 1-wt% CNTs	0 MPa	1.47	1.35	7.02%
PBS 8001	5.8 MPa	1.45	1.42	2.17%
PBS 8001+ 1-wt% CNTs	5.8 MPa	1.47	1.42	3.44%
PBS 8001+ 3-wt% CNTs	5.8 MPa	1.49	1.44	3.91%

The samples cured under a pressure of 5.8 MPa had significantly lower porosity. The porosity found in samples PBS 8001 and PBS+1-wt% pressed at atmosphere nearly doubled the porosity of those same sample types that were cured under a pressure of 5.8 MPa. As evidenced in Table 5 the samples cured at atmosphere had a substantially lower actual density than ideal density, suggesting a significant amount of voids within the volume of the sample. The sample pressed under a constant weight reduced the void within the volume, bringing the actual density closer to the sample's ideal density approximation.

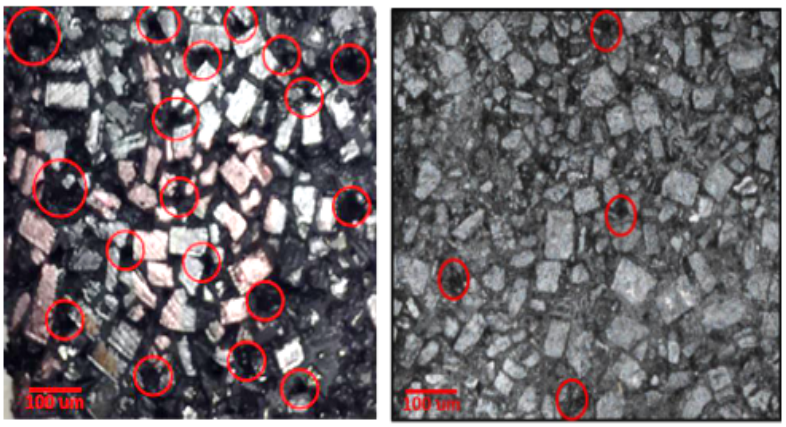

Figure 4.1: Surface voids in PBS 8001+ 1-wt% CNTs, un-pressed (left) and pressed at 5.8MPa (right). Images taken with a Nikon Eclipse MA100 Inverted Metallurgical Microscope at 5X magnification.

Optical microscopy provides visual documentation of the porosity predicted by our rule-of-mixtures estimation. In Fig. 4.1 two micrographs are shown of the surface features found in two PBS 8001+1-wt% CNTs samples, one pressed (left), and the other cured at atmosphere (right). These micrographs demonstrate the presence of voids in both un-pressed and pressed samples. The un-pressed samples with over 7% porosity exhibit a significant number of pores as highlighted by the red circles in Fig. 4.1 (left). The pressed samples contain a lower porosity, up to 3%, and the voids are less in number.

These images show the much-improved surface porosity due to applying pressure during the curing process. Samples with higher amounts of pre-existing voids also exhibit significantly weaker mechanical properties (see Table 5) and produce samples with inconsistent properties between iterations of the sample type. The increased presence of voids in un-pressed samples can be attributed to air pockets within the PBS mixture created during the pre-cure mixing process. Additionally, during hot temperature curing these air pockets can expand, increasing the void volume fraction. These voids are regions where temperature localization could form under mechanical insults. Curing under pressure minimizes this problem and produces samples with more reliable properties.

Quasi-static stress-strain response of neat PBS and CNT-enhanced PBS:

The stress-strain curves shown in Fig. 4.3 describe the unconfined quasi-static compressive behavior of samples with progressively higher concentrations of MWCNTs. These samples are pressed during the curing process, under a compressive pressure of 5.8 MPa. The compression data shown in Fig. 10 is presented as engineering stress-strain based on the Instron Universal test frame's 5kN load cell force readings and crosshead displacement. The unconfined quasi-static compression test procedure was adapted from an standard test method for axial compression of plastics and elastomers, ASTM D1621. The stiffness of test frame is several orders of magnitude higher than that of these polymer composites thus the compliance of the experimental setup was not of concern when calculating engineering strains. All compression experiments were done under atmospheric pressure and temperature and with a pre-load of 30 lb. or 133 N. Pre-loading ensures that the Teflon film used to minimize frictional forces on the top and bottom surfaces of the sample is compressed.

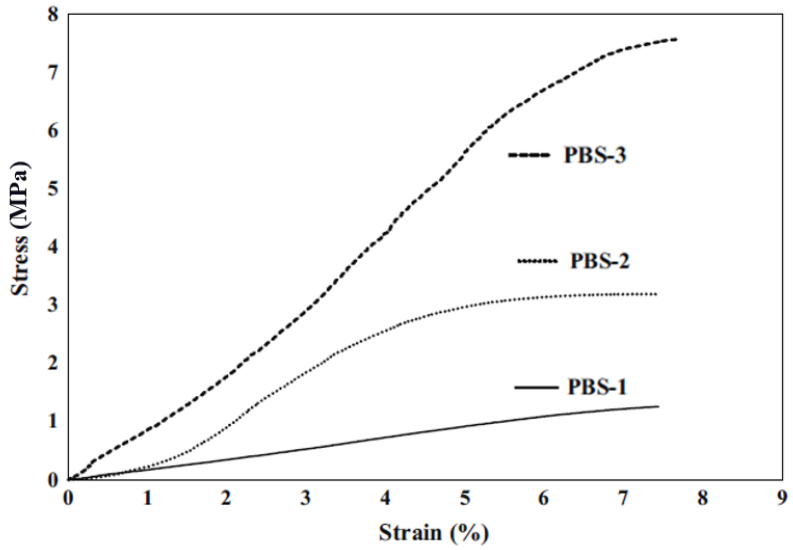

Figure 4.2: Uniaxial and unconfined quasi-static compression tests of PBS samples synthesized by Kidane et al. PBS-2 has a similar composition to PBS 8001 and exhibited a compressive young's modulus of 90 MPa and a yield strength of 2.7 MPa. PBS-1, PBS-2, and PBS-3 are composed of 80%, 85%, and 90% by sucrose by weight, respectively. Note that the units of stress are in MPa/MPa.

In Fig. 4.2, an example of an unconfined quasi-static compression test of a HTPB-based polymer composites. Kidane and Ravindran synthesized HTPB-based PBS samples comparable in composition to the PBS samples

presented in this study. Manner et al., created Estane-based PBX samples using HMX, an explosive material. The PBS substitute behaves similarly to the PBX material, demonstrating on the efficacy of sucrose as a simulant explosive material. The following unconfined quasi-static results build from this work by enhancing strength properties of the binder-phase of the composite.

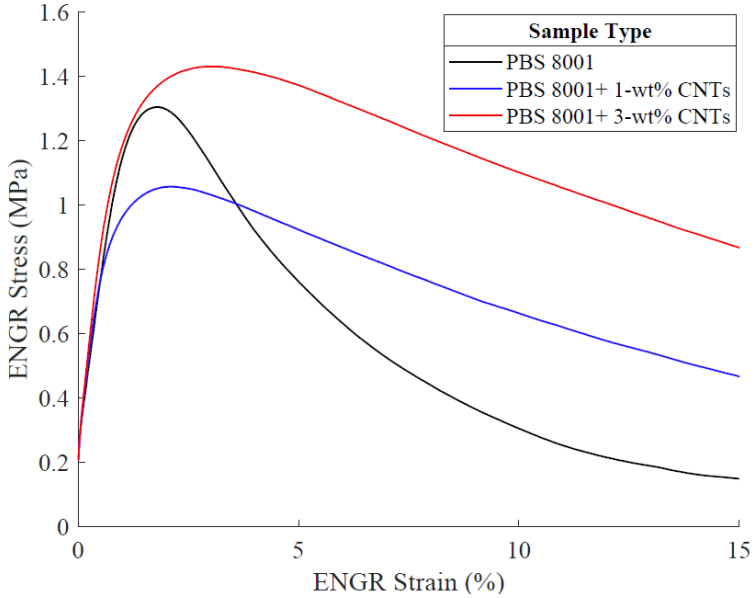

Figure 4.3: Stress-strain curves of PBS 8001, PBS 8001+1wt% CNTs, and PBS 8001+3wt% CNTs under quasi-static uniaxial compression. These samples were pressed at 5.8 MPa during cure.

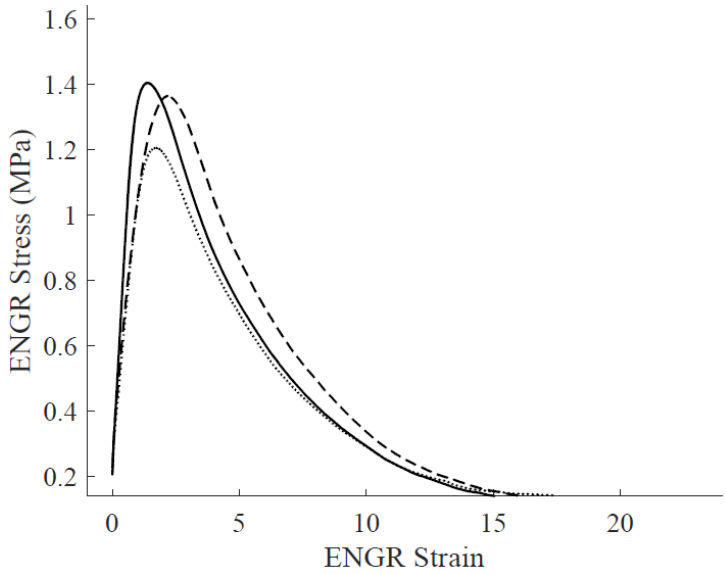

Figure 4.4: Stress-strain curves of PBS 8001 (pressed at 5.8 MPa during cure) under quasi-static uniaxial compression. These samples were pressed at 5.8 MPa during cure. Stress-strain curves of nominally identical PBS 8001 samples shown.

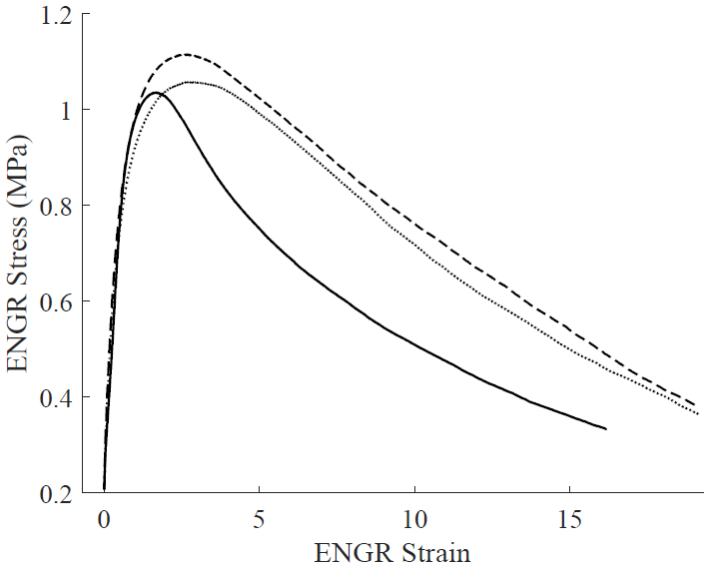

Figure 4.5: Stress-strain curves of PBS 8001+1%wt CNTs (pressed at 5.8 MPa during cure) under quasi-static uniaxial compression. These samples were pressed at 5.8 MPa during cure. Stress-strain curves of nominally identical PBS 8001+1%wt CNTs samples shown.

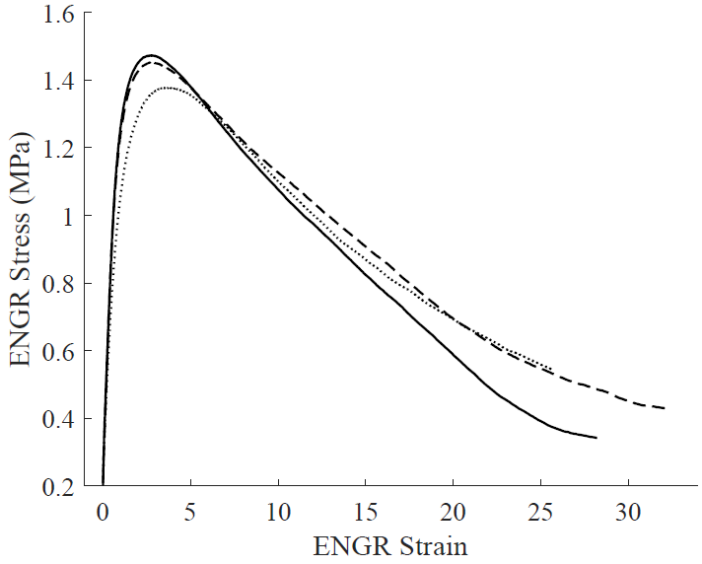

Figure 4.6: Stress-strain curves of PBS 8001+3%wt CNTs (pressed at 5.8 MPa during cure) under quasi-static uniaxial compression. These samples were pressed at 5.8 MPa during cure. Stress-strain curves of nominally identical PBS 8001+3%wt CNTs samples shown.

The engineering stress-strain curves shown in Fig. 4.3 represent an average of three compression tests performed on samples of the same sample type (repeated test results are shown in the appendix). As the concentration of MWCNTs is increased within the binder-phase of the composite the maximum strain before failure increases. Additionally, the tangent modulus in the post-yield region decreases as the curve flattens. These observations indicate an unexpected result of injecting CNTs into the composite; the bulk material becomes less brittle and exhibits more plastic-like deformation.

Table 4.2: PBS Unconfined Quasi-Static Compression Properties (pressed at 5.8 MPa)

Batch	Elastic Modulus (MPa)	Tangent Modulus (MPa)	Maximum Stress (MPa)	Strain-at-Max (%)
PBS 8001	121.8 ± 6.2	-18	1.15 ± 0.12	1.7
PBS 8001+ 1-wt% CNTs	98.5 ± 4.7	-4.9	0.912 ± 0.13	3.2
PBS 8001+ 3-wt% CNTs	113 ± 2.4	-3.1	1.28 ± 0.08	3.9

In Table 4.2, the mechanical properties estimated from the stress-strain curves from Fig. 10 demonstrate significant changes as the concentration of MWCNTs increases. The compressive elastic modulus was estimated by applying a linear regression algorithm to the curve between 0.3% and 0.4% strain. The tangent modulus is estimated using the stress-strain data from a region between 1% and 5% strain. This measure assumes a uniaxial stress state during compression and that yield occurs at a point before the maximum stress. This modulus measurement, shown in Table 4.2, demonstrates an increase in plastic-like behavior post-yield; the modulus is reduced by 50% in both PBS 8001+1-wt% CNTs as well as PBS 8001+3-wt% CNTs. Another feature of note is the mild decrease in strength and elastic modulus when 1-wt% CNTs are added to the binder. This may be due to the deleterious affect CNTs have on the cure of the polymer mixture. Saeb and co-workers have shown, in epoxy composites, that the addition of CNTs does have an effect on the cure kinetics of polymers.

Fractography of neat PBS and CNT-enhanced PBS:

The macroscale optical analysis performed here documents the failure mechanisms occurring with each PBS 8001 sample type during unconfined quasi-static compression. A Nikon D5500 camera equipped with a macro lens recorded the failure behavior of each sample during and after compression testing. The simultaneous compression and imaging allowed for the viewing of important points in the deformation process, such as, yield and plastic flow. In order to facilitate higher image quality, the samples are polished on one surface to expose the sucrose crystals. The crystals themselves are up to 2 mm in size. The upside to performing in-situ macroscale imaging is that the images stay in focus even during deformation and failure, which is a common problem when imaging at the smaller scales. However, optical methods can only observe surface level failures effectively. This leaves the internal void and defect behavior unseen.

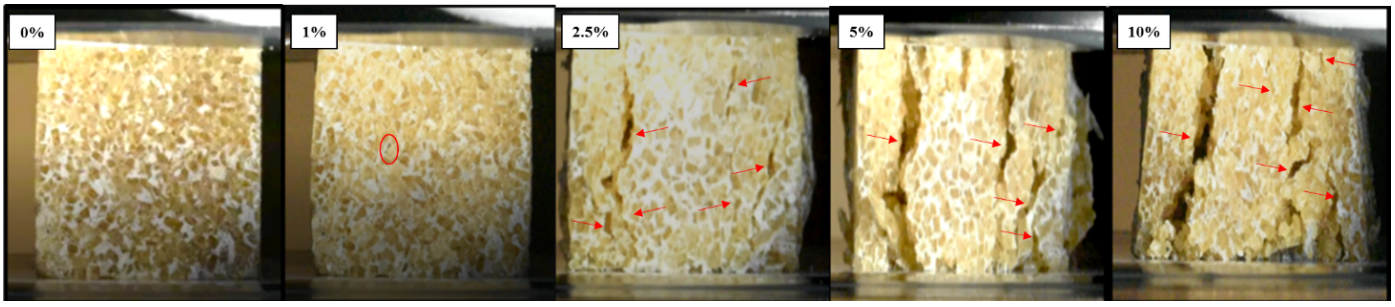

Figure 4.7: In-situ images of PBS 8001 under quasi-static uniaxial compression. Strain value on top left corner of each image is the real-time strain level.

The first signs of failure seen during compression are mainly crystal de-bonding. Figure 4.7 shows the first signs of crystal de-bonding in the PBS 8001 samples and begin at roughly 1% strain. At the interfaces where crystals begin to de-bond, the likelihood of fracture formations and voids in the sample increases. The rate at which the crystals de-bond increases as the stress increases, and in the PBS 8001 samples this leads to large

fractures at around 2% strain. These large vertical cracks span the entire face of the sample. Crystal de-bonding is the most prominent failure mechanism present under low strain rate compression. The stages of failure shown in Fig. 4.7 proceed in the following fashion:

1) Elastic deformation: the crystals begin to de-bond and slip (1% strain)
2) Yield: crystal-binder de-bonding continues to produce visible fractures (2.5% strain)
3) Post-yield: several vertical fractures form, spanning the surface of the sample (5% strain)

The sample begins to deform as early as 1% strain and reaches a maximum stress level at approximately 2.5% strain. The large-scale crystal de-bonding and crack growth of the PBS 8001 baseline and lack of plastic flow indicates the behavior of a brittle material. The brittle failure of the PBS 8001 is not only due in part by crystal-binder de-bonding, but is also by crystal-crystal interaction. PBS with higher stiffness have shown to exhibit higher amount of crystal-crystal interaction. The de-bonding that occurs often results in void growth, binder fracture, and crystal fracture. In Fig. 4.7, the behavior shows that while the binder is deforming, the crystals slip and rotate to fit with the deforming binder, often creating new voids.

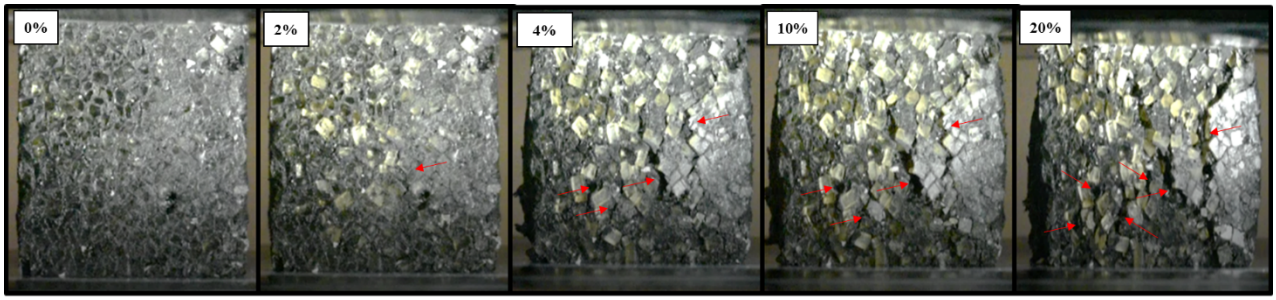

Figure 4.8: In-situ images of PBS 8001+1-wt% under quasi-static uniaxial compression. Strain value on top left corner of each image is the real-time strain level.

The CNT-enhanced samples fail in a similar manner as the PBS 8001 counterparts, however at later points on their respective stress-strain curves. The PBS 8001 baseline samples reach maximum load at about 1.7% strain, but the PBS 8001+ 1-wt% CNT samples do not reach their maximum load until around 3.4% strain. This shows that the strain to yield of the CNT samples is nearly double that exhibited by PBS 8001. At 5% strain, Fig. 4.8 shows a PBS 8001+ 1-wt% CNT sample beginning to develop vertical fractures due to crystal de-bonding. At the same strain-level, PBS 8001 is almost at its full disintegration point. The presence of the CNTs within the binder seems to enhance the ductility of the polymer matrix. The CNTs slow down void formation and growth due to crystal-binder de-bonding.

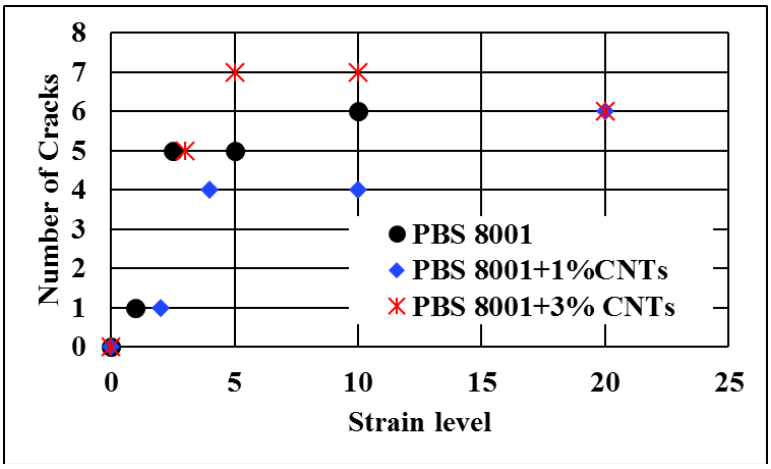

Figure 4.9: Number of cracks at each strain level as presented in Fig. 11, 12, and 14. Crack was subjectively identified as visible damage with a length of at least 2 mm.

In Fig. 4.9, the PBS 8001 samples reach a maximum number of large and visible cracks at a smaller strain than the enhanced samples. The behavior of the enhanced PBS 8001 samples implies that the MWCNTs increases the resistance to damage under uniaxial compression. An important observation from the CNT-enhanced samples is the de-boding seen between crystals and binder. The crystals de-bond from both the binder and the CNTs. Figure 4.9 shows the PBS 8001+ 1-wt% CNTs samples at several key stages of failure:

1) Uncompressed
2) First visible signs of crystal de-bonding (3% strain)
3) First visible signs of fracture (5% strain)
4) Fracturing extends through body of sample (10% strain)

The sucrose crystals are yellow, while the CNT enhanced binder is black. The crystal slip from the CNT binder occur as the sucrose grains appear in higher number during compression. This indicates a minor amount of bonding occurs between the phases of the CNT-enhanced composite. This implies that the CNTs have good dispersion within the binder and the CNT-Matrix bonds are significantly stronger than the CNT-Sugar bonds. The minimal binder-sucrose bond produces a structural skeletal matrix that in effect carries the majority of the load, allowing the crystal phase to slip with minimal friction and without fracturing. For comparison, in PBS 8001, crystal phase fractures occur more prominently due to bearing a higher portion of the load.

In the CNT-enhanced samples, this enhanced structural integrity of the binder maintains some of its strength even after the crystals begin to de-bond. In PBS 8001, the binder begins to form cracks once the crystals begin de-bonding. However, this does not happen as quickly or as prominently in the CNT-enhanced samples. In fact, the CNT enhanced samples show small cracks through 10% strain. At the same strain-level, PBS 8001 loses all structural integrity.

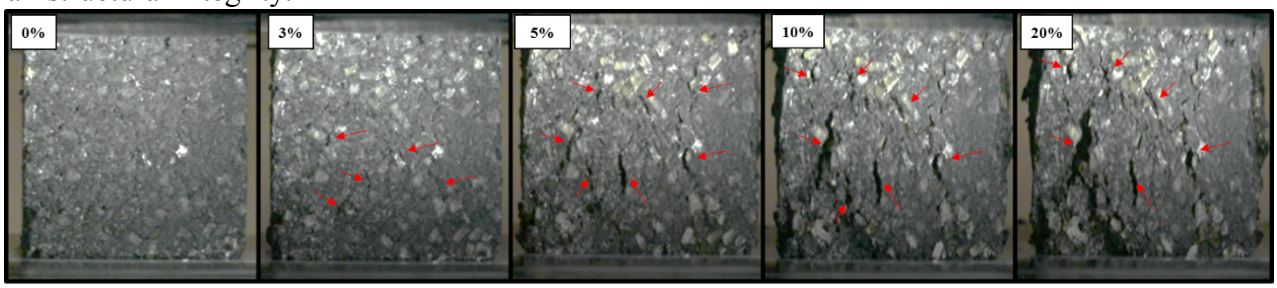

Figure 4.10: In-situ images of PBS 8001+1-wt% under quasi-static uniaxial compression. Strain value on top left corner of each image is the real-time strain level.

Fracture and failure still occurs in the CNT enhanced samples, however, they do not fully fail until over 20% strain. The CNTs produced a structural skeletal effect that increases the ductility of the binder, promoting plastic flow. This slows some of the crystal de-bonding, and mitigates brittle fractures from forming. Incorporating increased amounts of CNTs in a polymer matrix has been shown to promote improved fracture resistive behavior in polymers in previous work.

The deformation behavior of the PBS 8001+ 3-wt% CNTs compares favorably to the PBS 8001+ 1-wt% CNTs. Both CNT-enhanced samples behave similarly in the post-maximum stress region. The effects of the CNTs holding the binder together and providing enhanced structural stability are even more apparent in the PBS 8001+ 3-wt% CNT samples. It is also important to note the formation of a shear band during deformation of the CNT samples (see Fig. 4.10). Shear banding occurs mainly during the deformation of ductile materials. Shear banding often precedes failure since and commonly produces on 45-degree angles from the direction of applied stress. Adding CNTs into the binder seems to have produced a binder that is more capable of transferring the load away from the crystals, producing less voids, cracks, and changes the fracture behavior from brittle to ductile.

Table 4.3: Properties of PBS Samples from unconfined quasi-static compression tests

Batch	Press Force (lbs.)	VVF (%)	Elastic Modulus (MPa)	Max Stress (MPa)
PBS 8001	0 MPa	6.4	8.5	0.32
PBS 8001+ 1-wt% CNTs	0 MPa	>7.0	8.64	0.51
PBS 8001+ 3-wt% CNTs	0 MPa	>7.0	12.1	0.72
PBS 8001	5.8 MPa	1.9	102	1.10
PBS 8001+ 1-wt% CNTs	5.8 MPa	3.4	97	0.85
PBS 8001+ 3-wt% CNTs	5.8 MPa	3.9	122	1.22

Batch	Elastic Modulus (MPa)	Post-Max Slope (MPa)	Maximum Stress (MPa)	Strain-at-max (%)
PBS 8001	90.13 ± 6.34	-26.19 ± 0.81	3.04 ± 0.06	3.59 ± 0.13
PBS 8001+ 1-wt% CNTs	100.67 ± 7.17	-16.21 ± 1.28	2.57 ± 0.14	2.89 ± 0.14
PBS 8001+ 2-wt% CNTs	114.83 ± 0.99	-28.53 ± 1.04	3.84 ± 0.10	4.33 ± 0.10
PBS 8001+ 3-wt% CNTs	80.77 ± 12.35	-27.67 ± 5.80	4.70 ± 0.33	5.69 ± 0.53

Measured thermal conductivity of neat PBS and CNT-enhanced PBS:

In Table 4.4, the thermal conductivity values found for PBS 8001 samples are presented. These results present a compelling case for MWCNTs enhancement properties of thermal conductivity in polymer binders. Particularly, the PBS 8001 + 3-wt% CNTs exhibit nearly a 50% increase in thermal conductivity. The addition of MWCNTs significantly changed the bulk properties of the composite material. In the proceeding sections, an in situ thermographic drop weight impact examination will demonstrate how this bulk property affects the thermal localization behavior of PBS 8001.

The temperature gradients are recorded using the FLIR 6752 MWIR camera. After steady state is achieved in the reference material, the camera records for two minutes. From this recording, temperature gradients from the materials can be analyzed.

Table 4.4: Thermal conductivity of PBS 8001

Batch	MWCNT Mass [%]	Thermal Conductivity [W/m-K]
Polymerized HTPB	0	0.251
PBS 8001	0	0.379
PBS 8001 + 1-wt% CNTs	1	0.573
PBS 8001 + 3-wt% CNTs	3	0.607

Thermomechanical response of neat PBS and CNT-enhanced PBS subject to drop weight loading:

In Fig. 4.11, the displacement data is shown as recorded by the magnetostrictive linear position sensor. This displacement data represents the top plate's displacement from rest. As the sample is loaded the top plate remains at rest. At a critical point, about 5ms, the test sample begin to deform. This is reflected in the plot as positive displacement of the top plate. The slope of this data between 6 and 8 ms can be interpreted as a loading rate. Due to the geometry of the samples this loading rate cannot be taken as a global strain measure.

However, the consistency of the displacement data between test runs and the linearity of the data suggests that equilibrium was achieved during impact.

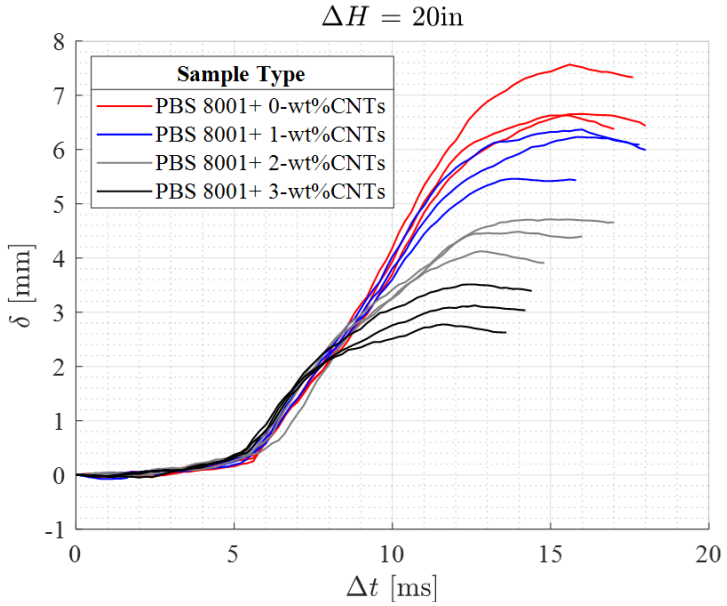

Figure 4.11: Dynamic displacement data for PBS 8001 samples and their variants tested under impact from a drop height of 20 inches.

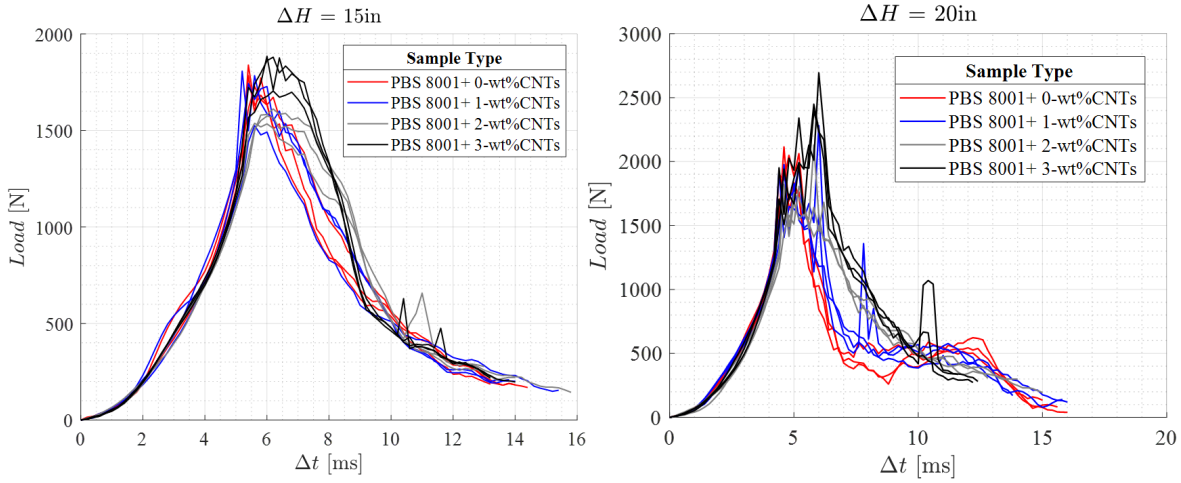

Figure 4.12: Dynamic load versus time data

The load data recorded during impact, shown in Fig. 4.12, proves that the sample reached an equilibrium state during impact. At such a state it can be assumed that any inelasticity and their subsequent thermal heating are due the stress wave moving through the sample and not due to any surface friction or inertial effects.

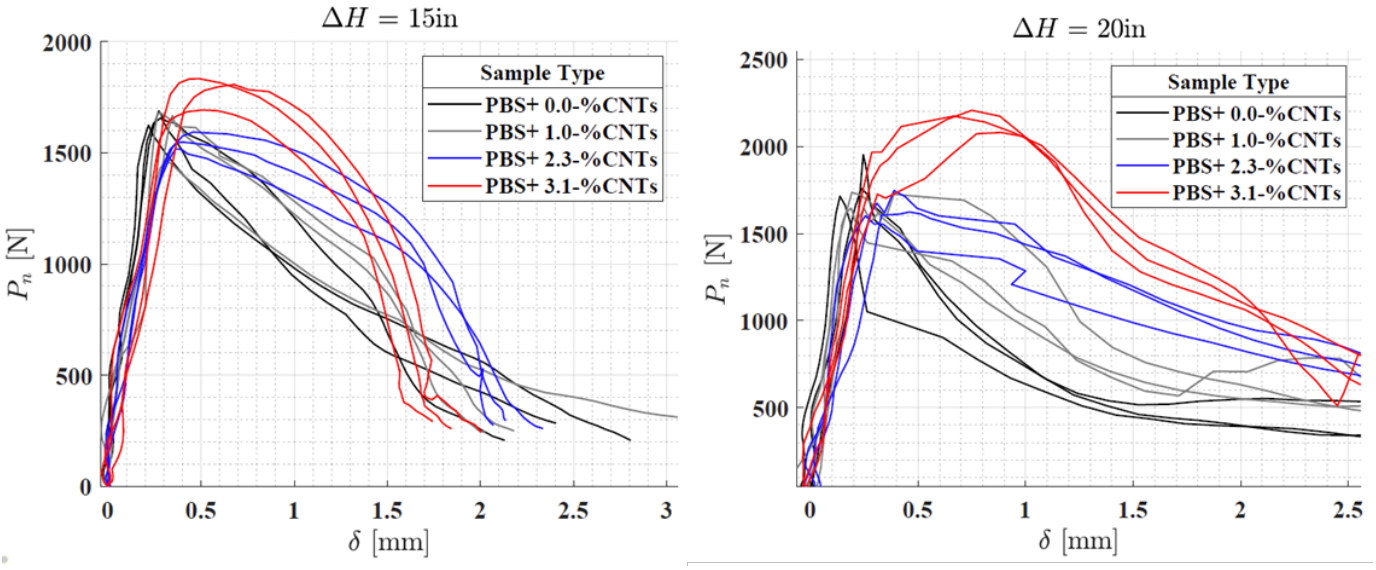

Figure 4.13: Dynamic load versus displacement

A summary of the dynamic behavior exhibited by PBS 8001 and its variants under drop weight impact is shown in Table 4.6. The confidence interval was calculated using a t-student distribution to account for small sample size (3 test samples per sample type) with unknown population mean and variance.

Table 4.6: Dynamic Loading, Height – 20 inches, N = 3 (95% Confidence)

Batch Name	Max Strain [%]	Max Load [lbs.]	Loading Rate [1/s]
PBS 8001	27.55±6.28	408.38±71.19	30.00±8.14
PBS 8001 + 1-wt% CNTs	23.59±4.75	384.64±25.63	28.95±2.67
PBS 8001 + 2-wt% CNTs	16.86±2.48	374.86±44.88	28.62±8.02
PBS 8001 + 3-wt% CNTs	12.00±3.92	488.40±43.78	22.66±7.01

The loading rate between different sample types is consistent; they lie within a 95% confidence interval. However, a significant increase in load and decrease in maximum strain is exhibited by the test samples as their enhancement increases. Similar trends appear in the dynamic summary data, shown in Table 4.6, for samples tested with a drop weight height of 20 inches.

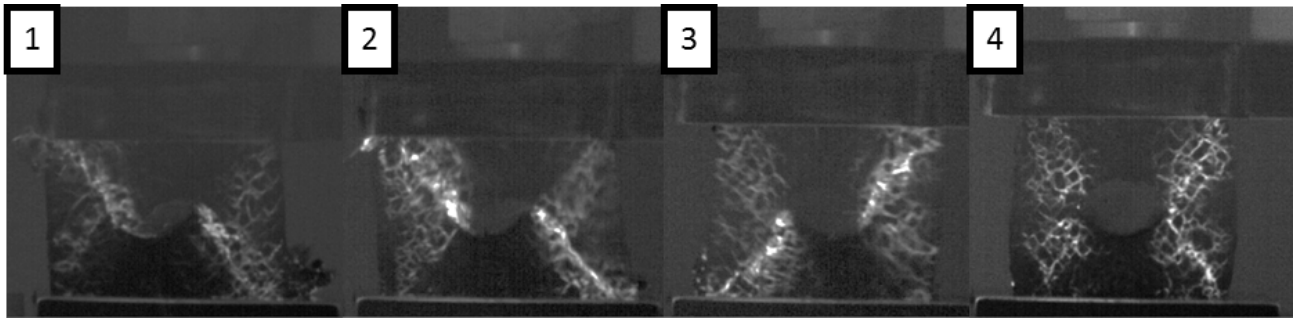

Figure 4.14: Infrared Images of PBS under impact from a drop height of 20 inches.

The following image, shown in Fig. 4.14, captures the temperature localizations at a time point near the point of maximum displacement. In some cases, this point coincides with the point of maximum temperature. The temperature localizations follow the same near 60^0 shear band damage lines shown in Fig. 4.15. Additionally, the thermal localizations occur among the interfacial boundaries between crystal and binder phases of the

composite. In some cases, localizing path follows these interfacial regions, implying thermal heating due to inelasticity occurring exclusively in the binder phase.

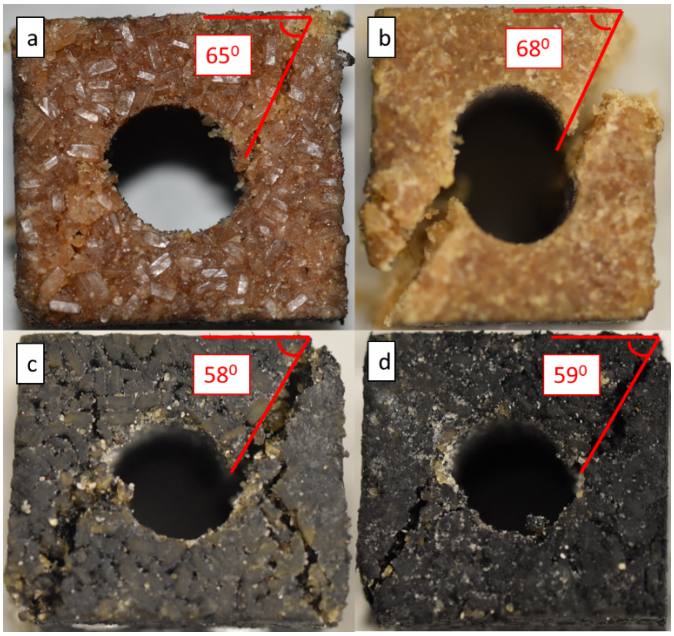

Figure 4.15: Post-impact images of test samples. (a) PBS 8001 tested at 15in (b) PBS 8001 CNTs tested at 20in (c) PBS 8001 +1%-wt CNTs tested at 20in (d) PBS 8001 +2%-wt CNTs tested at 20in

Displayed in Fig. 4.15 are post-mortem images of test samples that exhibited macro-level damage. In general, the damage occurred in $55^0 \sim 68^0$ shear bands. Test samples PBS 8001+1%wt CNTs, +2% wt CNTs, and +3% CNTs, tested with a 15 in drop weight height did not show significant damage. PBS +3% wt CNTs samples did not exhibit any macro-level damage in either drop weight height application.

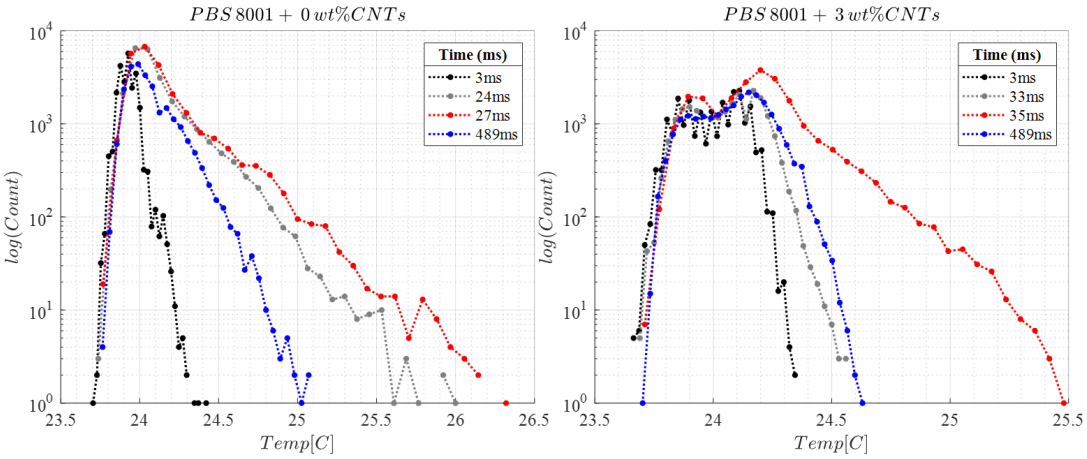

Figure 4.16: Temperature distribution transient evolution

The plots shown in Fig. 4.16 represent the distribution of temperature at four different time intervals during impact. The temperature examined was taken exclusively from the sample face. Background data was ignored using an Eulerian frame of reference. The temperature data shown in black represent the baseline temperature profile of the sample before impact. The data in grey represents the temperature distribution at

the time period before the maximum temperature was observed (temperature points shown in red). Due to the relatively low frame rate of the FLIR IR camera only one or two frames were captured before this maximum temperature point. The blue data points represent the temperature distribution at the last recorded frame.

The plot shown in Fig. 4.17 displays the peak temperature observed at each frame captured by the FLIR IR camera during impact. The starting data point represents the maximum temperature observed through the impact event. The transient evolution of the peak temperature exhibits a near exponential decay. As the CNT enhancement increased the rate of decay increases as well. In the time region between 0 and 100ms a sharper 'elbow' can be observed in the data. This implies that the peak temperature localization more effectively diffuses away as the enhancement increases.

In these transient temperature distributions, the test samples with CNT enhancements exhibit a faster return to its baseline temperature profile. This implies that the thermal conductivity is having a significant effect on the materials ability to diffusive thermal localizations to a room-temperature steady state after 0.5 seconds.

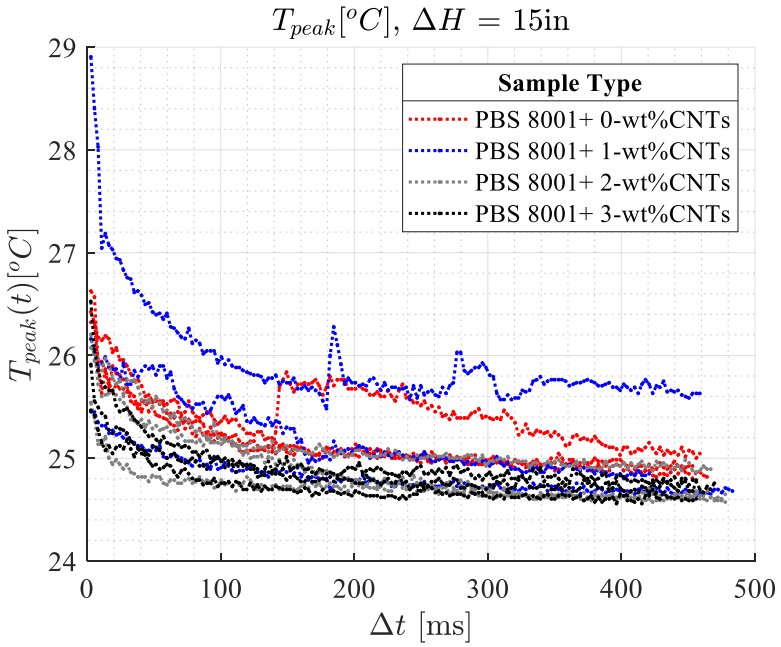

Figure 4.17: Transient evolution of peak temperature
Samples were tested with a drop weight height of 15 inches

A similar trend can be observed in Fig. 4.18. Here the average is taken of the temperature profile at each frame capture during impact by the FLIR IR camera. This data is plotted from the point of maximum average temperature observed to the end of the infrared video capture. The difference in decay in not as pronounced as seen in the peak temperature data. However, this measure also indicates that the CNT-enhancement is having an effect on the rate of diffusion on the sample face during impact.

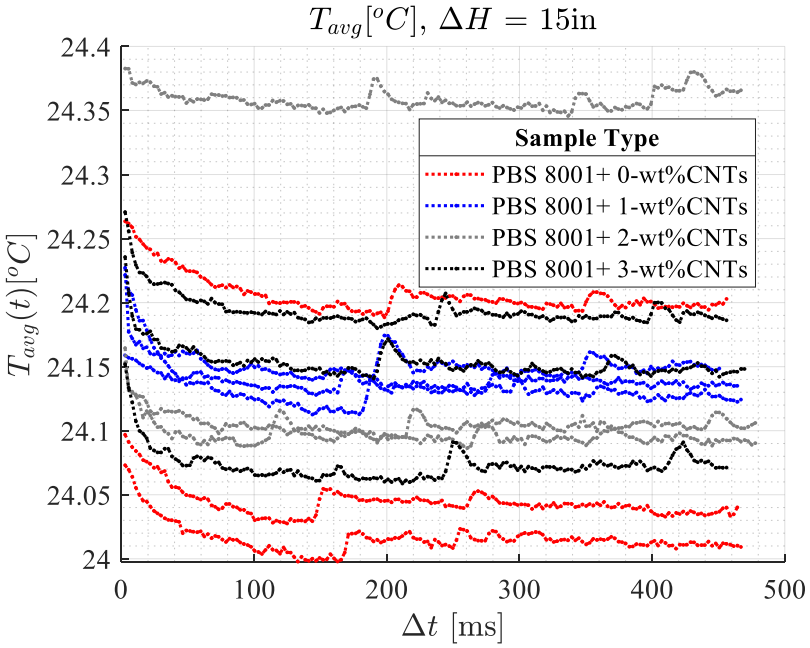

Figure 4.18: Transient evolution of average temperature
Samples were testing with a drop weight height of 15 inches

V. KEY FINDINGS FROM MESOSCALE CALCULATIONS

Over 100 mesoscale calculations stemming from this grant are reported in the dissertation of Babak Ravaji, which may be provided upon request. A select subset of these calculations are provided below.

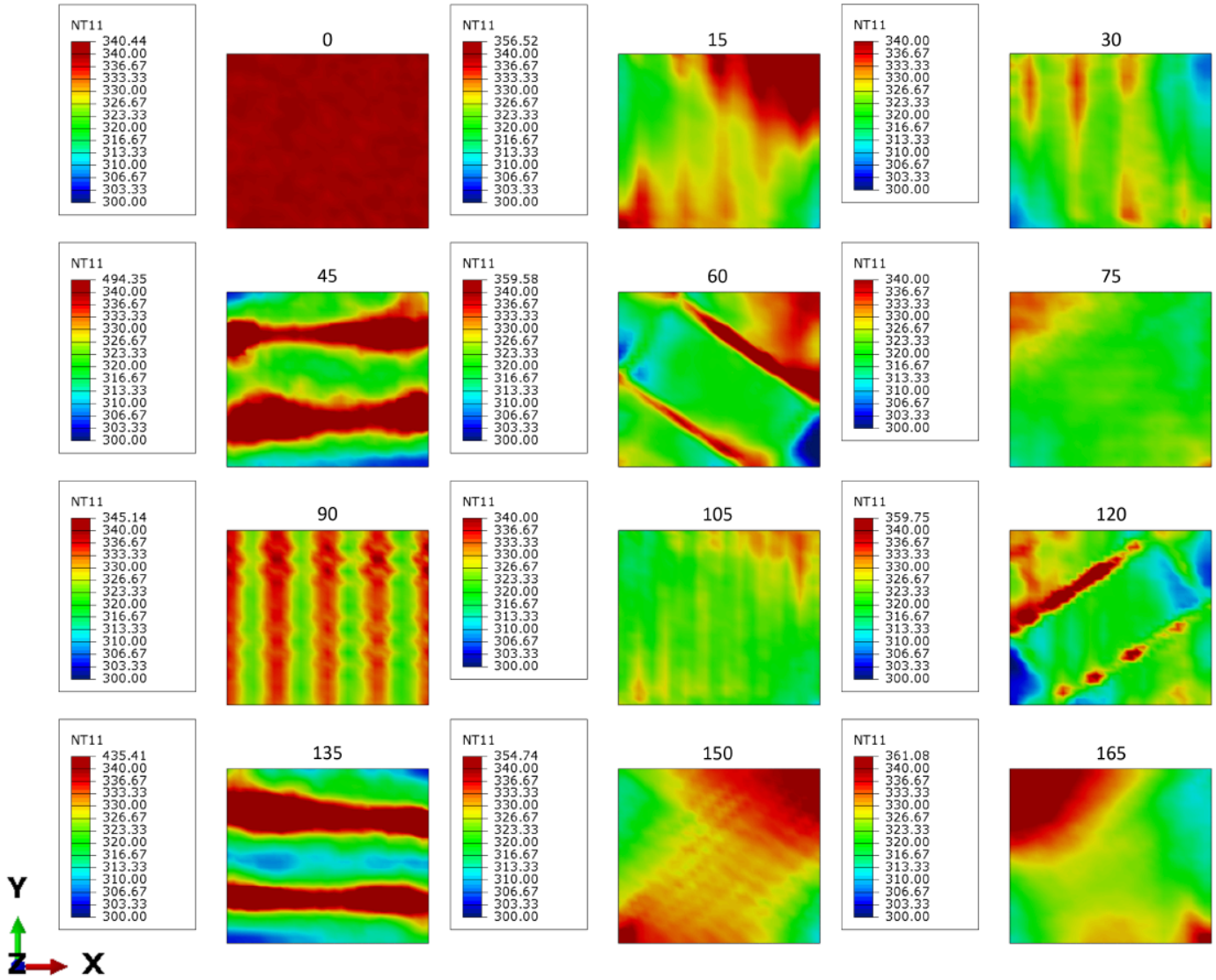

Figure 5.1: Temperature evolution (K) in porous single crystal RDX subject to 12% nominal vertical strain at strain rates of 2500/s. Fixed and symmetric boundary conditions are applied on the bottom and side surfaces, respectively. The crystal orientation of the top left simulation is such that the x-axis coincides with the <100> slip direction. The orientation dependence of the temperature is demonstrated by rotating the material clockwise in 15-degree increments.

The predicted spatial distribution of temperature in porous single crystal RDX is shown in figure 5.1. Remarkably, RDX manifests strongly anisotropic thermomechanical behaviors under uniaxial deformation. Note that the temperature legend is limited from 300 K to 340 K in Fig. 5.1. All temperatures above 340 K are shown in dark red. The peak stresses and peak temperature rises are shown in Table 5.1. All calculations have an initial porosity of 9%. The value of the porosity in deformed configuration is shown in the Table 5.1 as well.

Table 5.1: Summary of peak stresses, peak temperatures, and final porosities in porous single crystal RDX subject to 12% nominal strain at a strain rate of 2500/s.

Orientation (°)	Mises (MPa)	Pressure (MPa)	Porosity (φ)	Temperature change (K)
0	1134	2238	0.071	28.3
15	1384	2275	0.072	22.3
30	1433	2288	0.073	21.8
45	1485	2291	0.073	20.8
60	1717	2325	0.074	16.6
75	1691	2314	0.074	18.2
90	1559	2279	0.073	22.9
105	1691	2314	0.074	18.2
120	1717	2325	0.074	16.6
135	1485	2291	0.073	20.8
150	1433	2288	0.073	21.8
165	1384	2275	0.072	22.3
180	1134	2238	0.071	28.3

Figure 5.2 shows the predicted effect of binder conductivity on hot-spot formation in polymer bonded explosives subject to macroscopic uniaxial deformation. Conventional PBX shown in Figure 5.2(a) develops significantly hotter hot-spots than PBX with the same mechanical properties, but with a thermally conductive binder phase that is able to quickly transport heat from hot-spots as they are forming. This figure provides a proof-of-concept for the proposed multifunctional materials-by-design strategy.

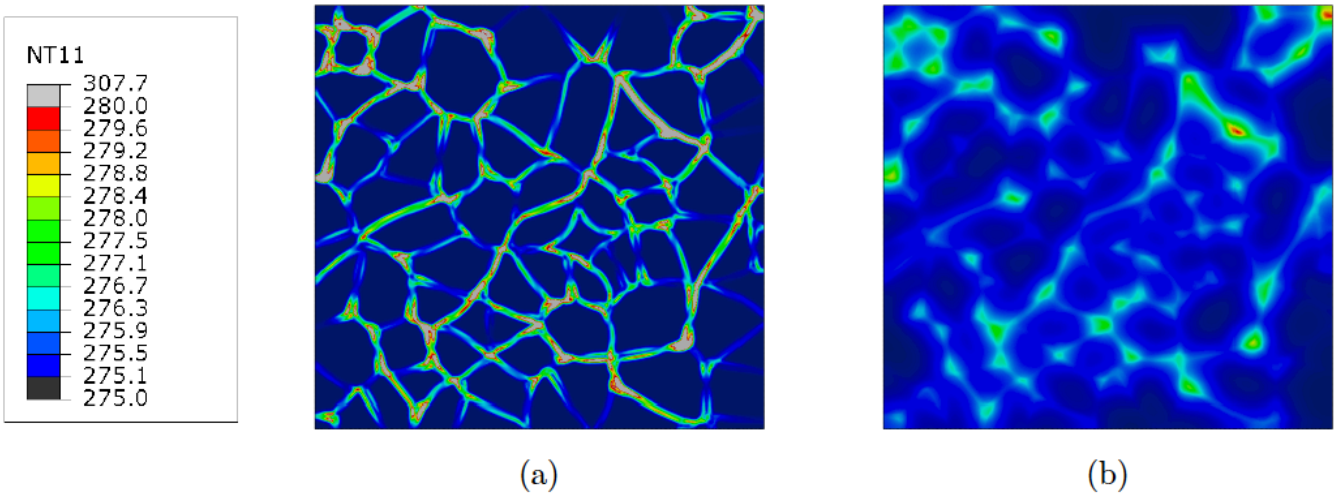

Figure 5.2: Effect of binder thermal conductivity on hot-spot evolution in PBX for (a) binder phase with thermal conductivity of baseline Estane and (b) a CNT-enhanced binder phase with 100X the baseline thermal conductivity.

Dozens of parametric calculations showing the effect of loading rate and length scale are combined in one contour map shown in Fig. 5.3. The same colors in the map represent similar thermal situations. The light blue in the middle of the graph shows situations where the thermal conduction plays the most important role. For macroscopically uniform loading, the length scale is governed by the microstructure, e.g. the size of

energetic crystals for a fixed volume fraction of crystals. Generally higher loading rates and larger crystal sizes give rise to adiabatic situations. Slow strain rates and small crystal sizes give rise to adiabatic situations.

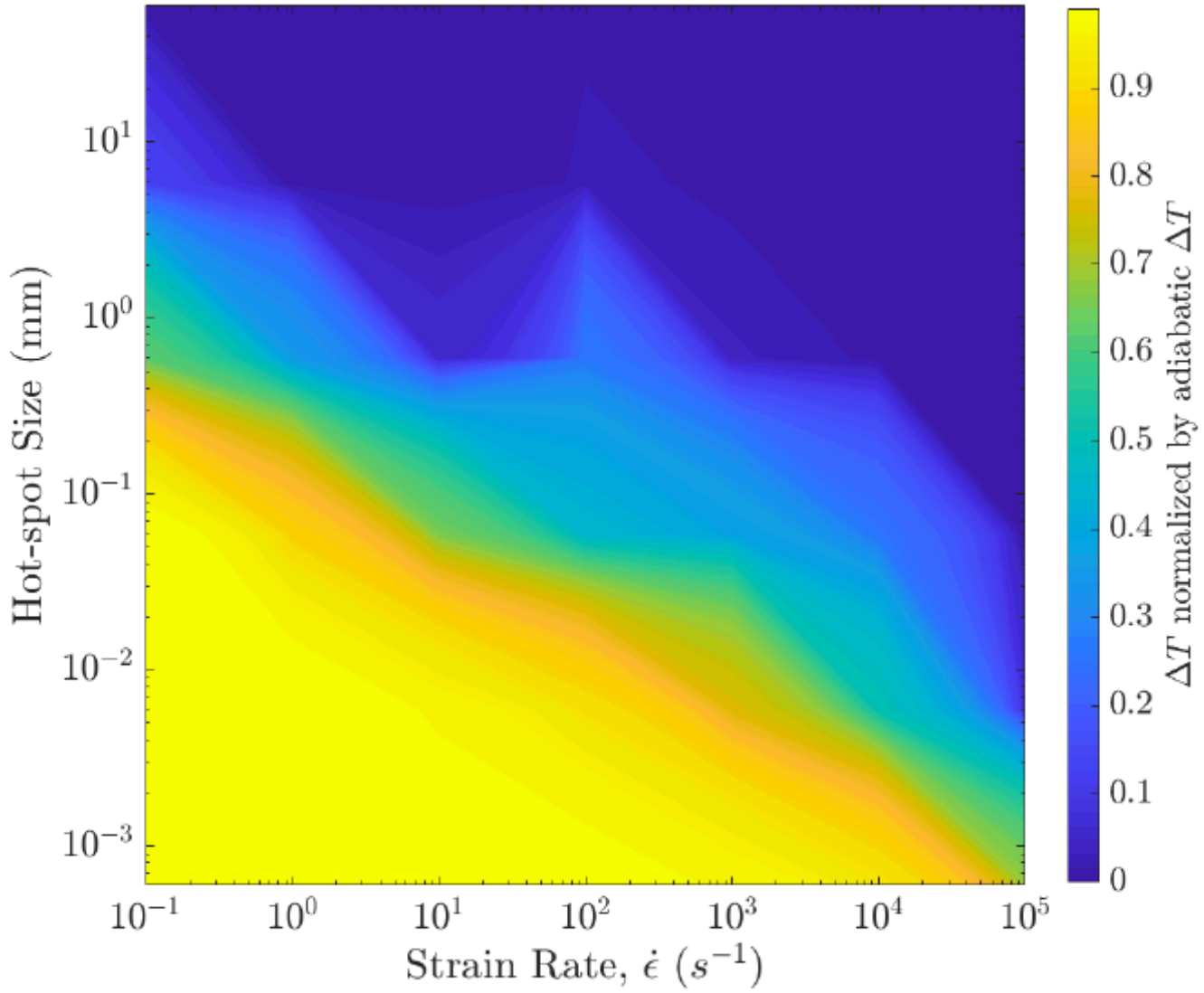

Figure 5.3: Combined effect of length scales and timescales on the importance of thermal conduction in hot-spot formation. Bright yellow regions are nearly isothermal. Dark blue regions are nearly adiabatic. Intermediate colors demonstrate loading scenarios for which enhancement of PBX thermal conductivity may have significant effects on ignition sensitivity.

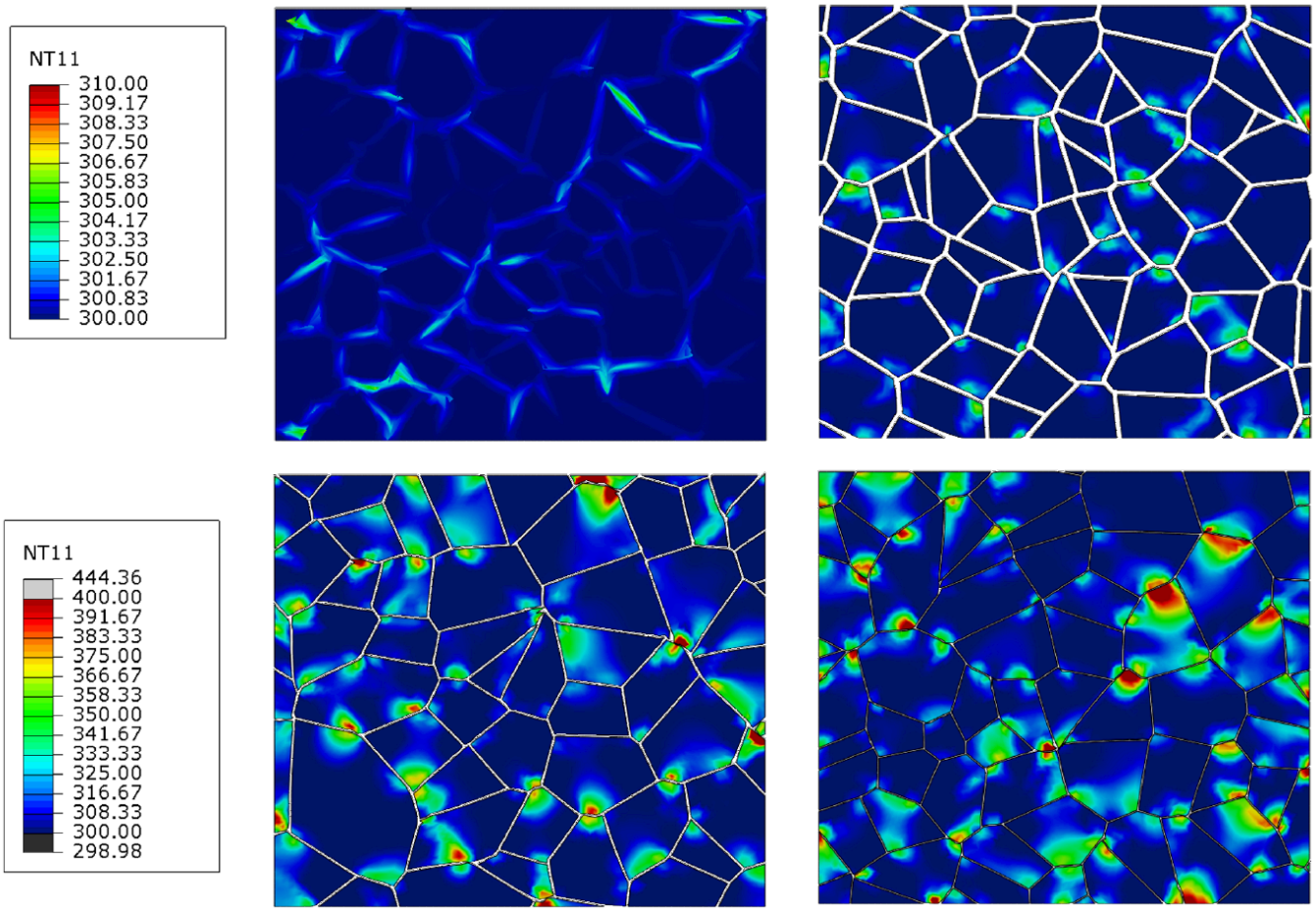

Figure 5.4: Temperature (K) distribution in PBX with (a) 70%, (b) 80%, (c) 90%, and (d) 95% crystal volume fractions. The representative volume elements are subject to 12% compression at a nominal strain rate of 1000/s.

Fig. 5.4 shows temperature distribution in the multi grain model for different volume fraction. The key difference between Fig. 5.4 and Fig. 5.2 is that here heat generation is due to plastic deformation and porosity collapse in the energetic crystals experience as well as due to viscoelastic dissipation in the binder phase. For this particular loading configuration, most of the heat generation occurs due to the porosity reduction and porosity collapse within the crystals.

As shown in Fig. 5.4 deformation induced heating in the crystal phase is significant only when the RDX volume fraction is over 80%, for this particular loading configuration. Below such crystal volume fractions, the soft binder in between crystals acts like a cushion and prevents intense stress concentrations within the crystals.

VI. ACKNOWLEDGMENTS

This material is based upon work supported by the Air Force Office of Scientific Research under award number FA9550-16-1-0204. Any opinions, finding, and conclusions or recommendations expressed in this material are those of the authors and do not necessarily reflect the views of the United States Air Force.